Innovative Characterization of Amorphous and Thin-Film Silicon for Improved Module Performance

Annual Subcontract Report: 28 April 2005 – 27 April 2006

J. David Cohen
Department of Physics and Materials Science Institute
University of Oregon, Eugene, Oregon

Prepared for the National Renewable Energy Laboratory

under Subcontract No. ZXL-5-44205-11

NREL Technical Monitor: B. von Roedern

PREFACE

This Annual Technical Progress Report covers the work performed at the University of Oregon for the period 28 April 2005 - 27 April 2006 under NREL Subcontract Number ZXL-5-44205-11. The following personnel participated in this research program:

NAME	TITLE	WORK PERFORMED
J. David Cohen	Principal Investigator	Program Manager
Shouvik Datta	Research Associate	Properties of NREL HWCVD a-Si,Ge:H alloys
Peter Hugger	Research Assistant	Properties of United Solar nc-Si:H materials
Pete Erslev (Half Time)	Research Assistant	Construction of new transient photocapacitance work station. Studies of Cu(InGa)Se_2 photovoltaic devices.

TABLE OF CONTENTS

LIST OF ILLUSTRATIONS

Page

LIST OF TABLES

EXECUTIVE SUMMARY

Our work under NREL Subcontract ZXL-5-44205-11 during Phase I has focused on three areas of study. First, we used transient photocapacitance (TPC) spectroscopy, transient photocurrent (TPI) and drive-level capacitance profiling (DLCP) to characterize the electronic properties of hydrogenated nanocrystalline Si (nc-Si:H) within a set of working n-i-p solar cell devices produced at United Solar Ovonics Corporation. Because the nc-Si:H layers in these more recent samples appear to be somewhat more intrinsic than those studied previously, with electron carrier densities estimated to lie below 10^{15} cm^{-3}, we were able to obtain a definite deep defect response in our DLCP measurements for some of the samples. Surprisingly, this defect signal was observed to decrease after light-soaking rather than increase. At the same time, the minority (hole) collection fraction, as revealed by the TPC spectra, was significantly reduced. This led us to propose a microscopy model to explain these observations. This model assumes that the relative electron potentials of the amorphous regions are shifted downward as a result of light-soaking, presumably from some type of light-induced charge separation across the phase boundaries of these mixed phase materials.

Second, we continued our studies of the lower filament temperature HWCVD a-Si,Ge:H alloys being developed at NREL. These samples have revealed very good electronic properties. However, some later samples were of definite poorer quality and this appeared to be a result of excess oxygen contamination. The source of this contamination was identified and eliminated in the Fall, 2005, and we were then able to obtain a series of samples for study with different levels of oxygen introduced in a controlled manner using a variable air-leak. Surprisingly, these samples did *not* show a deterioration of electronic properties as a result of increasing oxygen levels. Moreover, the samples with moderate levels of oxygen actually revealed smaller Urbach energies, to below 40meV in one case. We also began examining the kinetics of light-induced degradation and annealing in these samples. It appears that these kinetics are somewhat different than those obtained in high quality PECVD a-Si,Ge:H films. In particular, the metastable deep defects anneal away over a much narrower ranges of temperatures than the PECVD a-Si,Ge:H films, suggested a narrower range of energy barriers for metastable defect recovery.

Third, we applied both admittance and DLCP measurements to a set of CIGS photovoltaic devices that were obtained from Miguel Contreras at NREL. We examined eight devices that varied in their level of performance, from about 14.4% to nearly 17.5% efficiency. Admittance measurements carried out at zero volts applied bias did not reveal significant differences among this set of films. In particular, they did not reveal any variations in the deep acceptor capacitance step that some studies have found to be an indicator of device efficiencies. However, the DLC profiles on this set of NREL samples did indicate major differences. In particular, the DLCP determined defect density obtained under forward bias conditions, probing the defects in the region closest to the barrier interface, appeared to be reasonably well correlated to the device efficiencies across this set of samples.

1.0 INTRODUCTION

The work carried out during Phase I under NREL Subcontract. ZXL-5-44205-11has focused primarily on three subject areas. First, we have been continuing to evaluate the nanocrystalline Si material under development at United Solar Ovonics Corporation (USOC) which will be denoted in this report as nc-Si:H. It is hoped that such materials may ultimately be able to replace one of a-Si,Ge:H layers in an amorphous silicon triple junction device. Previously our junction capacitance methods revealed a substantial amorphous silicon component to these nc-Si:H materials and indicated that under light induced degradation the minority carrier collection fraction was substantially reduced. Whereas previously most of our results were obtained on specialized sandwich type devices in which the nc-Si:H layer was sandwiched in between two a-Si:H cladding layers, the samples studied during the past year were actual nc-Si:H n-i-p working solar cell devices. The behavior of the nc-Si:H layer in these devices was found to be qualitatively identical to that in the sandwich devices examined previously. Further important results have been achieved regarding the details of the light induced degradation process, and a tentative model is proposed to account for the observed behavior.

Our second major focus has been in the continuing evaluation of amorphous silicon-germanium alloys produced by the hot-wire CVD growth process at NREL. This method holds some potential for higher deposition rate Ge alloy materials with good electronic properties. Last year we found that a series of NREL HWCVD a-Si,Ge:H films deposited using lower filament temperatures possessed superior electronic properties. However, a series of samples produced after the end of 2004 exhibited poorer properties that were tentatively blamed on increased levels of oxygen contamination. The oxygen contamination problem was solved at NREL, and this past year we explored the effects of oxygen at varying levels introduced intentionally using a controlled air leak-valve.

Finally, we began a new project to utilize our measurement methods to characterize the properties of copper indium-gallium diselenide (CIGS) based photovoltaic devices. Our work on CIGS materials is supposed to account for roughly 30% of our work under our Thin-Film Partnership Subcontract. The goal of this work is to try to identify the reasons for the vastly different performance levels of laboratory based devices (which now can exceed 19% efficiency) compared to CIGS devices produced by growth processes more suitable to large scale manufacturing (these devices rarely exceed efficiencies of 13%). To begin we have been examining a few series of NREL CIGS cells in which the performance level varies, to try to identify differences in the electronic properties of the CIGS absorbing layer that might be responsible. One key issue we have identified concerns the spatial distribution of electronic properties across the CIGS film that seems to correlate with the cell performance level.

2.0 SAMPLES

2.1 UNITED SOLAR NANOCRYSTALLINE SILICON

Two sets of nc-Si:H sample devices were obtained from United Solar (B. Yan) during the past Subcontract year. The first was a series of six nc-Si:H devices which we received in May 2005, shortly after the beginning of our new Subcontract. Three of these were deposited by MVHF at a rate of 6Å/s, and the other 3 were deposited by the RF process at a somewhat lower rate. The MVHF samples were all n-i-p devices deposited onto SS coated with a textured Ag/ZnO back reflector and were finished with 0.05cm^2 ITO top contacts. Two of these devices exhibited relatively high levels of degradation (about 15%) while the third exhibited very little degradation. The three RF nc-Si:H samples were fabricated in three different device structures: One was a n-i-p device with a Ag/ZnO textured back reflector, one was a n-i-p device on bare stainless steel, and one was a sandwich device: SS/a-Si:H/nc-Si:H/a-Si:H where the a-Si:H capping layers were 0.21μm thick. For all 6 devices the nc-Si:H layer was just under 1μm thick. The characteristics of these samples are summarized in Table I. The goal for this series of samples was to find out whether we could distinguish different electronic properties for the high degradation and low degradation films, and whether we could obtain consistent results on the RF samples independent of their different device structures.

A second series of five nc-Si:H samples was received from United Solar in January 2006. All of these were n-i-p devices. Two of these were deposited on specular stainless steel (SS) substrates, and three employed textured Ag/ZnO substrates. All the nc-Si:H intrinsic layers for this sample series were deposited using a modified VHF glow discharge process with a thickness roughly 1.5 μm. For all samples, ITO dots with an area of 0.05 cm^2 or 0.25 cm^2 were deposited on the p layer as top contacts. In addition, three of the samples were grown using a H_2 dilution profiling process to control crystalline size and volume fraction distribution. The other two

Table I. May 2005 United Solar nc-Si:H sample device series.

Sample Number	Substrate	Structure	Comment
2B 10505	SS/Ag/ZnO	n-i-p, all nc-Si:H	Low Degradation
2B 10514	SS/Ag/ZnO	n-i-p, all nc-Si:H	High Degradation
2B 10521	SS/Ag/ZnO	n-i-p, all nc-Si:H	High Degradation
RF 13512	SS/Ag/ZnO	n-i-p, all nc-Si:H	Low Degradation
RF 13510	Specular SS	n-i-p, all nc-Si:H	Same as 13512
RF 13511	Specular SS	a-Si:H/nc-Si:H/a-Si:H	Same as 13512

Table II. January 2006 United Solar nc-Si:H sample series. All were n-i-p devices with roughly 1.5μm thick I-layers. The cell performance parameters are listed.

Sample No	Substrate	J_{SC} (mA/cm^2)	V_{OC} (volts)	FF	Eff (%)	H_2 Dilution
14027	Ag/ZnO	26.5	0.469	0.581	7.22	Profiling
14036	SS	17.38	0.448	0.568	4.42	Profiling
14037	Ag/ZnO	25.99	0.429	0.512	5.71	Constant
14038	SS	17.36	0.451	0.531	4.16	Constant
13993	Ag/ZnO	24.39	0.548	0.641	8.57	Profiling

samples were grown using a constant H_2 dilution process for comparison. The structures that were deposited on textured substrates were nearly identical to actual end-product devices and so constituted material tested in its optimized geometry. Indeed, as can be seen from the cell performance parameters are listed in Table II, this sample set included one sample with an efficiency that exceeded 8.5%.

2.2 NREL HOT-WIRE CVD AMORPHOUS SILICON-GERMANIUM ALLOYS

During our previous Subcontract we had received from Yueqin Xu and Harv Mahan at NREL a series of seven a-Si,Ge:H samples deposited using the hot-wire CVD process with Ge fractions of 0, 15, 29, 47, 63, 81, and 100at.%. These were characterized and many of their basic electronic properties were reported in our 2005 Final Report. At the beginning of 2005 we received two additional a-Si,Ge:H samples with Ge fractions of 29 and 47at.% which were not characterized until the beginning of our current Subcontract. These two samples were found to have significantly higher oxygen contamination levels than the previous set and we were asked to compare their properties with the samples of the same Ge fractions (L1306 and L1307) that we had characterized previously. The growth characteristics of these samples (L1306, L1307, L1430, and L1431) are listed in Table III. All of the above samples were deposited onto specular stainless steel substrates, and a semi-transparent Pd contact was thermally evaporated on top of the intrinsic layer to provide a Schottky junction for our capacitance based measurements.

At the end of July we received five more samples: L1549(29%Ge), L1550(47%Ge), L1551(15%Ge), L1552(60%Ge), and L1553(another 29%Ge). These were deposited onto both the standard specular stainless steel substrates as well as onto p^+ crystalline Si substrates that had been specially prepared at the University of Oregon. These latter samples were designed to provide a better evaluation of the minority carrier collection properties of these HWCVD

Table III. Growth parameters for the intrinsic a-Si,Ge:H layers deposited by HWCVD.

Sample Number	Ge Fraction (at.%)	Substrate	i-layer Thickness (μm)	Gas Ratio $\frac{GeH_4}{(GeH_4+SiH_4)}$	Final Substrate Temperature	Growth Rate (Å/s)	E_{04} (eV)	E_{Tauc} (eV)
L1306	29	Stainless steel	1.60	12%	293°C	1.78	1.66	1.50
L1430	29	Stainless steel	1.73	12%	305°C	2.4	1.64	1.50
L1549	29	p^+ c-Si (100)	1.47	12%	295°C	1.63	1.65	1.50
L1307	47	Stainless Steel	1.44	25%	292°C	2.00	1.47	1.32
L1431	47	Stainless Steel	2.27	25%	305°C	3.15	1.46	1.32

a-Si,Ge:H films. This is because we could then obtain TPI spectra using the buried p^+ rectifying heterojunction rather than the top Pd Schottky contact. This was important since TPI spectra on Schottky barrier devices often give a distorted picture of the sub-band-gap response. To date only one of this series of samples has been examined in detail (L1549). Its growth characteristics have been included in Table III.

The effects of oxygen contamination on these HWCVD deposited a-Si,Ge:H films was examined in more detail after the source of the contamination was finally determined and eliminated in the Fall, 2005. This then provided an opportunity to understand to what extent controlled changes in the level of oxygen contamination would affect the electronic properties of these samples. Therefore, another series of four a-Si,Ge:H alloy samples were deposited using a controlled leak valve to introduce a systematic variation in oxygen level during the HWCVD process. The growth parameters for this set of samples are listed in Table IV. These films were deposited simultaneously on both specular stainless steel and p^+ c-Si substrates. SIMS

Table IV. Growth parameters of a-Si,Ge:H samples in which a controlled air-leak was employed to vary the level of oxygen contamination.

Sample	Air leak Flow rate (sccm)	Gas Ratio $GeH_4/(GeH_4+SiH_4)$	Thickness (microns)	Initial Substrate Temp (°C)	Final Substrate Temp (°C)	Growth Rate (Å/s)
L1628	0.00	0.19	1.80	204	289	2.00
L1630	0.02	0.19	1.75	204	289	2.08
L1629	0.06	0.19	1.60	204	284	2.05
L1631	0.20	0.19	2.20	204	275	2.82

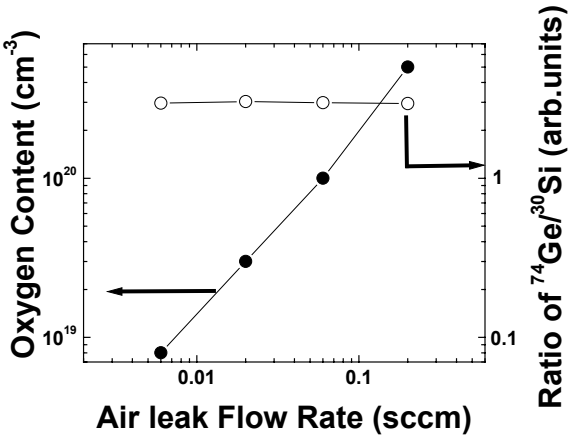

Figure 1. Oxygen content in NREL HWCVD a-Si,Ge:H films and their relative fractions of Ge with respect to Si as measured by SIMS. Note the systematic increase in the oxygen level in the fillm with increase air leak flow rate as well as the nearly constant fraction of Ge in this series of samples. Data corresponding to 'no intentional air leak' was plotted against an imaginary flow rate of 0.006 sccm.

measurements were carried out and indeed revealed a systematic increase of oxygen contamination as the air leak was gradually increased to 0.2sccm. Figure 1 shows the relative content of oxygen in the samples and germanium fraction with respect to Si. At the same time, these SIMS measurements indicated that the N content (<$4x10^{16}$ cm^{-3}) remained nearly constant.

2.3 NREL CIGS SAMPLE DEVICES

For the current Subcontract under the Thin-Film Partnership program, our Statement of Work indicated that we would devote roughly 30% of our effort to CIS thin-film photovoltaics, and 70% to silicon-based thin film technologies. Our stated goal in our CIGS work is to apply our measurement techniques to try to understand differences between the best laboratory cells, and those fabricated using processes better suited for manufacturing. To begin, we have been examining laboratory CIGS devices with high levels of performance, and this Subcontract year will report what we have learned from a set of high performance NREL CIGS devices that were obtained in July, 2005, from Miguel Contreras.

Table V. NREL CIGS devices from 3 depositions chosen for detailed characterization using our experimental methods. The area of each sample device was 0.406 cm^2.

Device Number	V_{OC} (volts)	J_{SC} (mA/cm^2)	Fill Factor (%)	Efficiency (%)
C1919-11 Cell 3	0.630	32.95	71.43	14.833
C1919-11 Cell 4	0.642	32.51	68.99	14.393
C1813-21 Cell 3	0.657	33.26	76.08	16.613
C1813-21 Cell 4	0.664	32.67	77.82	16.888
C1813-21 Cell 6	0.667	33.19	77.52	17.168
C1924-1 Cell 4	0.724	30.82	78.19	17.449
C1924-1 Cell 5	0.717	30.81	77.44	17.118
C1924-1 Cell 6	0.714	30.95	77.07	17.039

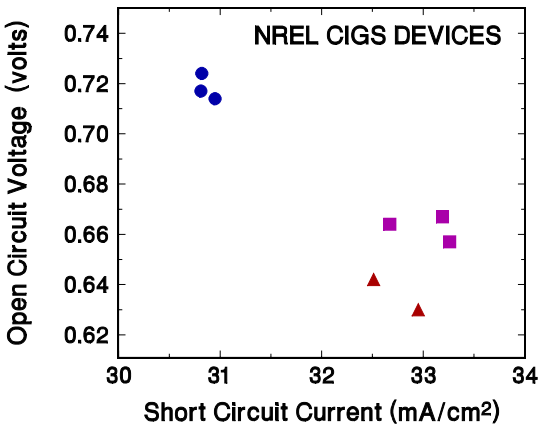

FIG. 2. Open circuit voltage vs. short circuit current for the eight CIGS devices listed in Table I: ▲ for the C1919 devices, ■ for the C1813 devices, and ● for the C1924 devices.

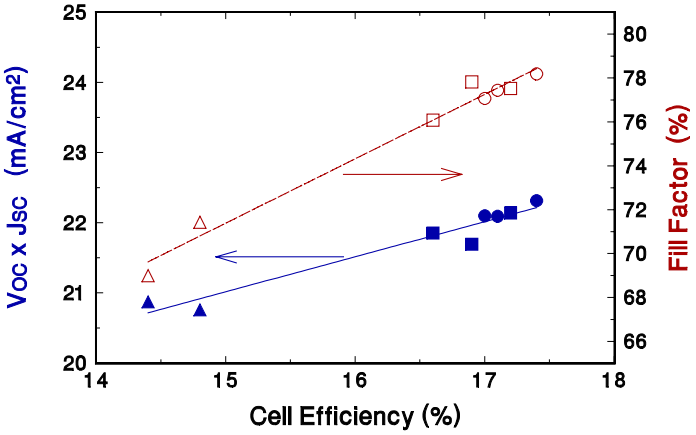

FIG. 3. Relationship of V_{OC}-J_{SC} products and Fill Factors to overall CIGS device efficiencies. This seems to indicate a dominant role for the Fill Factors in the overall device performance. The symbols shapes are used in the same manner as in Fig. 1.

Rather than characterizing only the best NREL CIGS devices, we thought it would be much more interesting to compare the results of our measurements on NREL devices with varying levels of performance. In that manner, we might be able to identify differences that might be correlated with those variations in performance. We therefore obtained three samples, each containing 6 devices, with average efficiencies in the 14-15% range (C1919-11), in the 16-17% range (C1818-21), and in the 17-18% range (C1924-1). Among the total of 18 devices, 4 or 5 seemed anomalous (primarily because of low shunt resistances) and we selected 8 of the remaining devices for detailed study that seemed to represent a good range of performance parameters. The performance parameters of the 8 devices we chose to characterize in detail, using admittance, DLCP profiling, and CV profiling, are listed in Table V.

Some useful insight into the performance parameters of these 8 samples is obtained by examining the plots of Fig. 2 and 3. In Figure 2 we examine the relationship between the open circuit voltage and short circuit current, while in Figure 3 we examine the relation between the device efficiency and both the Fill Factor and the V_{OC}-J_{SC} product. Figure 2 indicates that the 3 devices from sample C1924-1 are somehow distinctly different from the other 5 devices in that they have significantly higher values of V_{OC} and lower values of J_{SC}. One contributing factor is the fact that the absorber in C1924-1 contains on average a slightly higher fraction of Ga than did samples C1813-21 or C1919-11. This is revealed in SIMS measurements used to deduce the Ga-to-In profiles that are displayed in Fig. 4.

Figure 3 indicates that the variation in efficiencies for these 8 devices is correlates most strongly with Fill Factor, but that the V_{OC}-J_{SC} product increases monotonically with device efficiency as well. There were no obvious correlations between device efficiencies and either the open-circuit voltage or short-circuit currents for this set of samples.

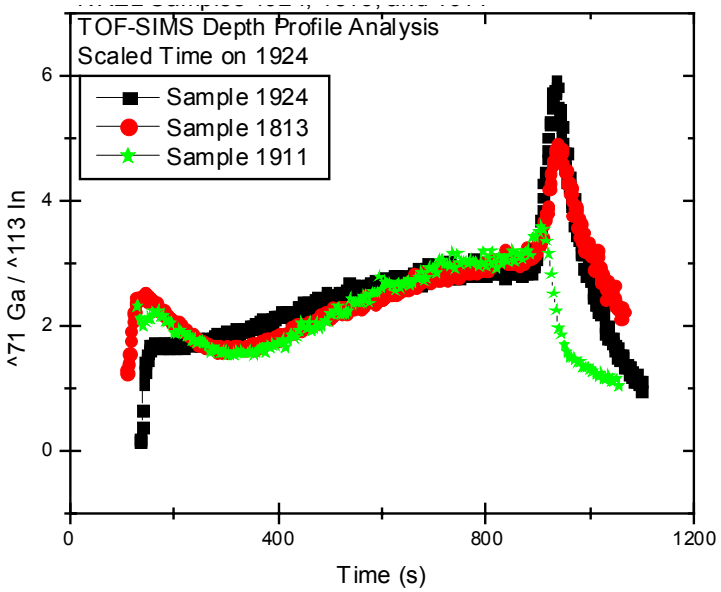

FIG. 4. SIMS determined spatial profiles of the Ga-to-In ratios for representative NREL CIGS sample devices from each of the three depositions. Note that these profiles for samples 1813 and 1911 appear nearly identical, but that the profile for sample 1924 indicates a slightly higher overall Ga fraction. These data were obtained using the TOF-SIMS instrument at the CAMCOR facility at the University of Oregon.

3.0 EXPERIMENTAL CHARACTERIZATION METHODS

The measurements employed in our studies rely on a set of experimental techniques which have all been described previously in some detail. They consist of (1) admittance spectroscopy as a function of temperature and frequency, (2) drive-level capacitance profiling, (3) transient capacitance spectroscopy, and (4) transient photocapacitance taken together with transient junction photocurrent spectroscopy. Here we will describe each method only very briefly and review what kind of information is obtained from each type of measurement.

3.1 ADMITTANCE SPECTROSCOPY

All of our sample devices contain a depletion region which is characterized as a function of temperature and frequency before we undertake the more sophisticated capacitance based measurements described in Sections 3.2 to 3.4 below. Such measurements provide us with an estimate of our film thickness (the temperature independent region at low T is simply related to the geometric thickness, d, by the formula $C = \varepsilon A/d$), and an Arrhenius plot of the frequency of the lowest temperature capacitance step (or conductance peak) *vs*. 1/T provides us with the activation energy of the ac conductivity, E_σ, which we identify with the Fermi energy position: $E_\sigma = E_C - E_F$.[1] These admittance measurements also give us an indication of the quality of the barrier junctions which allow us to pre-screen our samples for further study.

3.2 DRIVE-LEVEL CAPACITANCE PROFILING

The drive-level capacitance profiling method has been described in detail in many publications [2,3,4]. It is similar to other kinds of capacitance profiling in that it provides us with a density *vs*. distance profile; however, this particular method was developed specifically to

address the difficulties encountered in interpreting capacitance measurements in amorphous semiconductors. In this method we monitor the junction capacitance both as a function of DC bias, V_B, and as a function of the amplitude of the alternating exciting voltage, δV. One finds that to lowest order this dependence obeys an equation of the form:

$$C(V_B,\delta V) = C_0(V_B) + C_1(V_B)\,\delta V + ...$$

and that the ratio

$$N_{DL} \equiv \frac{C_0^3}{2q_e \varepsilon A^2 C_1} \qquad (1)$$

is directly related to an integral over the density of mobility gap defect states. For example, for n-type samples:

$$N_{DL} = \int_{E_c - E_e}^{E_F^o} g(E)dE + \textit{free carrier density} \qquad (2)$$

Here E_F^o is the bulk Fermi level position in the sample and E_e depends on the frequency and temperature of measurement:

$$E_e(\omega,T) = k_B T \log(\nu/\omega) \qquad (3)$$

Thus, by altering the measurement temperature (or frequency) we obtain information about the energy distribution of the defects and, by altering the applied DC bias, we can vary the spatial region at which we detect the defects in the sample. That is, we can spatially profile the defects as a function of the position from the barrier interface.

In our current studies we typically measured 100Hz to 10kHz profiles for a series of temperatures between 100K to 360K. These data may indicate either a low or high temperature limit for N_{DL}. In the former case the integral contribution in Eq. (2) is small so we identify N_{DL} as the free carrier density. In the latter case we obtain the *sum* of the deep defect density plus the free carrier density. This can thus provides us with a quantitative measurement of the deep defect levels. In addition, because of the profiling information also obtained, we are able to assess the spatial uniformity of the electronic properties in these samples.

3.3 TRANSIENT CAPACITANCE SPECTROSCOPY

The general method of junction transient measurements on amorphous semiconductors has been discussed in detail in several earlier publications.[1,5,6] The basic physics of all such measurements is illustrated in Fig. 5. We illustrate the situation for an n-type semiconductor with one discrete deep gap states within the space charge region of a Schottky barrier which is subjected to a voltage "filling pulse". This pulse causes a non-equilibrium (filled) occupation of gap state to be established. As time progresses, the initial steady-state population is recovered

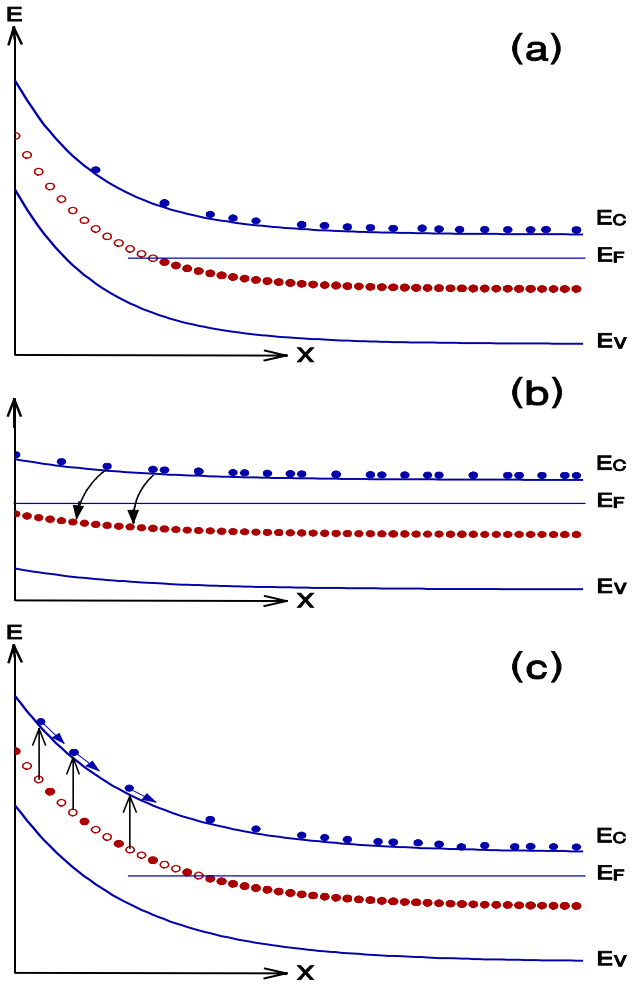

FIG. 5. Schematic diagram indicating the basic sequence of events in semiconducting junction transient measurements for an n-type sample:
(a) Junction under reverse bias in quasi-equilibrium showing the electronic occupation of gap states (solid circles) plus empty gap states above E_F in deep depletion (open circles).
(b) During voltage "filling pulse" gap states capture electrons from the conduction band.
(c) Reverse bias is restored and occupied gap states above E_F are slowly released to the conduction band due to thermal or optical excitation processes.

through the excitation of trapped electrons to the conduction band where they can then move out of the depletion region under the influence of the electric field. In the dark this process proceeds entirely by the thermal excitation of trapped carriers. However, this process can be enhanced through optical excitation and this is the basis of the photocapacitance and junction photocurrent techniques described in Section 3.4 below.

The re-equilibration can be observed by the redistribution of trapped carriers, either as a change in the *junction capacitance* (which occurs because the depletion region will contract as negative charge is lost and the positive charge density increases) or by monitoring the *current* which results from the motion of this charge. However, the observation of capacitance transients has one significant difference compared to current transient measurements: The dominant type of emitted carrier (electron or hole) can be identified by the *sign* of the observed change in capacitance.

3.4 TRANSIENT PHOTOCAPACITANCE AND PHOTOCURRENT

The methods of junction transient photocapacitance and photocurrent have been discussed

by us in great detail over the years in the literature [7,8,9] and also in previous NREL reports. They represent types of sub-band-gap optical spectroscopy and provide spectra quite similar in appearance to PDS derived sub-band-gap optical absorption spectra or to CPM spectra. Instead of detecting absorbed energy, however, our photocapacitance and photocurrent transient methods detect the optically induced change in defect charge within the depletion region. However, unlike the CPM method, both of our junction based techniques are not greatly influenced by the free carrier mobilities since, once an electron (or hole) is optically excited into the conduction (valence) band it will either totally escape the depletion region on the slow timescale of our measurement (0.1 to 1s) or be retrapped into a deep state and not escape. In most cases we assume that almost all of the optically excited majority carriers (electrons) *do* escape but, in general, only a fraction of the minority carriers (holes).

Because the photocapacitance and photocurrent measurements have different sensitivities to the loss of majority *vs*. minority carriers from the depletion region, a detailed comparison of the two kinds of spectra can be used to disclose the escape probability of the minority carriers from the depletion region.[7,10] This allows us to estimate the collection fractions of the minority carriers relative to the majority carriers. We are also able to distinguish whether optical excitation of defect states comes about because of the excitation of trapped electrons to the conduction band or because of the excitation of valence band electrons into an empty mobility gap state. This ability to distinguish electron from hole processes is unique among all the various types of sub-band-gap optical spectroscopies.

3.5 NEW PHOTOCAPACITANCE INSTRUMENTATION

Institutional matching funds for the current Subcontract including money to puchase a new scanning monochromator for the implementation of a new workstation for carrying out transient photocapacitance and photocurrent spectroscopy. Thus, in the summer, 2005, we purchases a McPherson Model 272 scanning monochromator together with a 250W tungsten-halogen lamp housing and power supply. The Model 272 is built around an f/2 holographic grating to provide higher intensity monochromatic light compared to our previously existing equipment. To expand our measurement capabilities even further with this new workstation, we incorporated a Linkham variable temperature sample probe. This enabled us to work with much larger samples (up to 3 x 5 cm^2) than had previously been possible with our glass flow cryostats.

The electronic components to complete this system had already mostly been acquired by my laboratory as back-up components for our two other photocapacitance workstations. The assembly of our new workstation was completed in the Fall, 2005, and has been available to take data since December 2005. Some of the first phototransient spectra obtained on this new system are displayed in Section 4 below (see Figs. 7 and 10).

4.0 PROPERTIES OF UNITED SOLAR NANOCRYSTALLINE SILICON

Simple variations in the growth parameters used to deposit hydrogenated amorphous silicon (a-Si:H) result in the growth of a form of hydrogenated microcrystalline silicon with crystallite sizes less than 10nm: Hydrogenated nanocrystalline silicon, nc-Si:H. We began an effort to understand this class of materials a few years ago, and some of our most successful results obtained on sample devices obtained from United Solar Ovonic Corporation were published in early 2006 [11]. Those results were obtained under funding by our previous NREL Subcontract and, because of our success to date, we are continuing to explore the electronic properties of nc-Si:H in our current Subcontract. Our goals in such studies include identifying the active defects, characterizing the carrier densities and transport properties, and trying to understand their light-induced degradation effects.

Whereas our earlier studies primarily employed specialized a-Si:H/nc-Si:H/a-Si:H sandwich test device structures, we have more recently been applying our capacitance-based characterization methods to a series of actual working nc-Si:H photovoltaic n-i-p devices of varying efficiencies. This allows us to more directly correlate the results of our measurements with actual device performance parameters. The most significant new results on such devices were obtained on the set of samples we received from United Solar in January, 2006, as listed in Table IV. In this set of samples the nc-Si:H intrinsic layers were deposited using a modified VHF glow discharge process with a thickness roughly 1.5 μm. Three of the samples were grown using a H_2 dilution profiling process to control crystalline size and volume fraction distribution. The other two samples were grown using a constant H_2 dilution process for comparison.

4.1 SUB-BAND-GAP PHOTOCAPACITANCE AND PHOTOCURRENT SPECTROSCOPY

For this set of five samples, two were deposited on specular stainless steel (SS) substrates, while three employed textured Ag/ZnO substrates. It is well known that substrate texturing enhances the spectral response of a device, especially for long wavelength photons. Although substrate texturing in these samples is clearly necessary to achieve the highest conversion efficiencies, texturing also significantly modifies the spectral response that we obtain in our sub-bandgap absorption spectra, and yields a somewhat distorted representation of the optical response of the nc-Si:H film itself. Figure 6 illustrates this point by comparing two transient photocurrent spectra for one textured substrate sample device (13993) with one without texturing (14036), both deposited in a similar manner with hydrogen profiling. The textured sample's flattened TPI response above roughly 1.3 eV, and its apparently broader Urbach energy below 1.1 eV are attributed to light-trapping effects. The specular sample is thus believed to show a much less distorted picture of the actual nc-Si:H optical absorption properties.

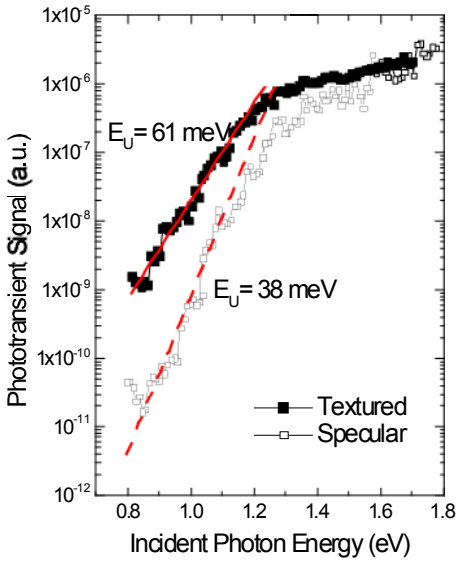

FIG 6. TPI spectra for nc-Si:H samples deposited on specular (solid symbols) and textured substrates (open symbols) are aligned at the higher optical energies for comparison purposes. The flatter optical response for the textured substrate sample above 1.2eV, as well as its apparently broader Urbach tail, are attributed to the light-trapping effect due to the textured substrate. Thus, the spectrum for the device deposited on the specular SS substrate is believed to more accurately represent the optical absorption properties of the intrinsic nc-Si:H layer itself.

Figure 7 displays 1.1 kHz TPC profiles for textured sample 13993 at three different temperatures. In each case, the TPC profile is aligned with the same representative TPI spectrum of this sample for reference (the TPI spectra for a given sample exhibit very little temperature variation). At 275 K and 285 K, we obtain TPC spectra that agree qualitatively well with spectra we obtained in previous work [11]. At 285 K the spectra clearly exhibit the amorphous phase present in these nanocrystalline devices by showing both a distinct a-Si:H bandtail near the amorphous silicon band-gap, as well as evidence of mid-gap states at lower incident photon energies. These spectra also exhibit the previously observed temperature variation in that, by decreasing the measurement temperature by 10 K (Fig. 2a), the TPC spectrum increases by more than a factor of 10 near 1.5 eV, indicating a corresponding decrease in the net hole collection at this photon energy. An even more dramatic change is observed when the temperature is raised to 295 K in this sample: the TPC signal actually becomes slightly *negative* near 1.5 eV. The absolute value of these negative data points are plotted in solid symbols in Fig. 2c. This negative signal indicates that *more* holes are being collected than electrons at these optical energies, probably because some of the photo-excited electrons become deep trapped and cannot escape during the 500 ms time window of our measurement. Therefore, the slight negative response in this region is not in itself so important; rather, it simply reflects that some electron trapping is occurring and that the hole collection is extremely good. Note that the signal again becomes positive at low optical energies since single-carrier excitation processes dominate in the deep defect region, and also positive at higher optical energies because the a-Si:H contribution with its lower hole collection fraction is larger in this region.

We examined the temperature dependence of the TPC signal in detail at an optical energy near 1.5 eV for this sample and found that the hole collection appeared to be thermally activated

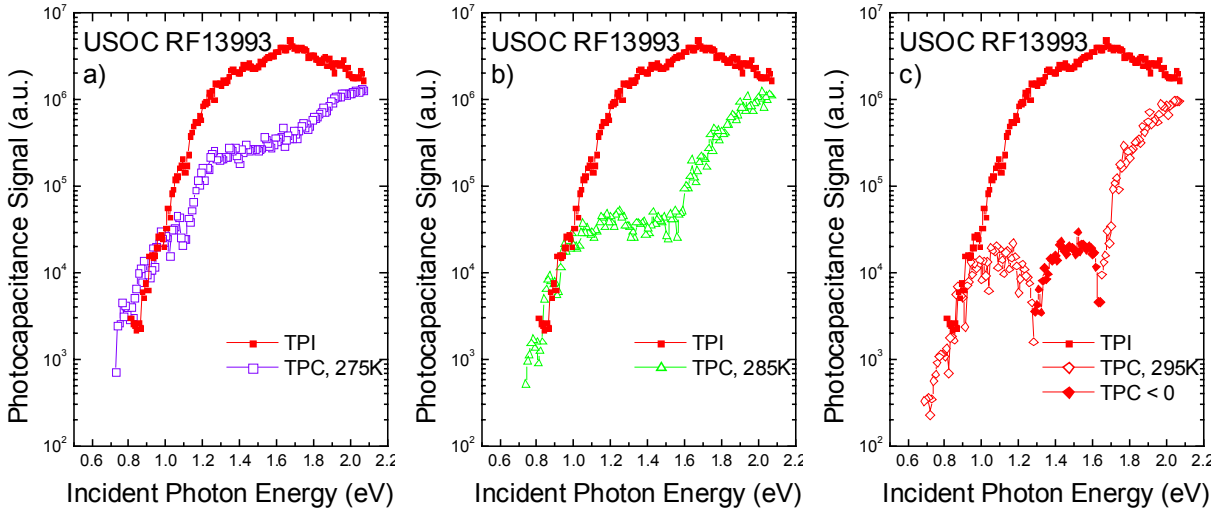

FIG 7. Comparison of TPI and TPC spectra at 275 K(a), 285 K(b), and 295 K(c) for the high-efficiency textured sample 13993. Nanocrystalline and amorphous phases are visible at low and high temperature, respectively. Note the negative TPC signal near 1.5 eV at 295 K.

as shown in Fig. 8. At lower temperatures, when the hole collection was strongly suppressed, we obtained an activation energy for hole collection that was very similar to that found previously [11]. However, in the temperature regime above 270K a significantly larger activation energy near 0.72 eV was exhibited. We tentatively attribute this to hole trapping into deep defects, possibly Si dangling bonds in the amorphous component. The fact that this deeper hole trapping accounts for only about 10% of the total (by comparing the magnitudes of hole collection at 200K and 300K) seems consistent with the idea that these deeper defects reside in the phase with lesser volume fraction in these materials; that is, the amorphous phase.

We also found that the relative hole collection was strongly sample dependent. For the three textured samples: 13993, 14027, and 14037, we determined the relative hole collection fractions at 300 K by aligning TPC and TPI spectra in the defect regime at 0.9 eV and then determining

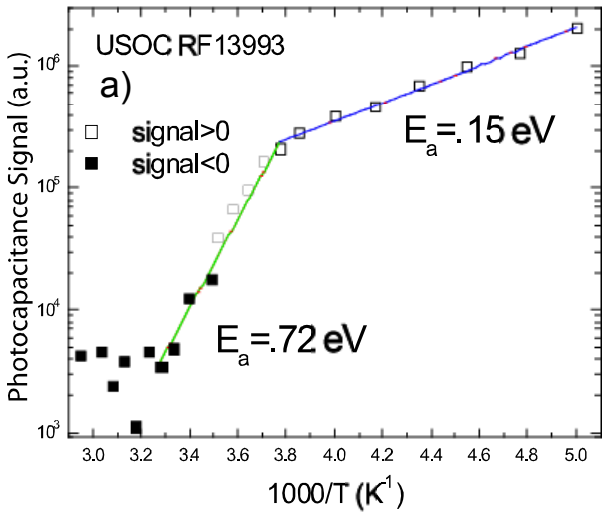

FIG 8. Variation of TPC signal with temperature at an optical energy near 1.5eV. A positive constant was added to the TPC signal to allow these data to be plotted on a logarithmic scale (the negative region is indicated by the solid symbols). We chose the constant which best extended the exponential dependence into the regime above 270K. This graph indicates thermally activated behavior for hole collection and, in contrast with previous results showing a single activation energy near 0.2eV, this sample reveals a second regime at higher temperatures with a significantly larger activation energy.

the average TPC/TPI ratio near an incident optical energy of 1.5 eV. This provided an estimate of the ratio $(n\text{-}p)/(n+p)$, from which the ratio p/n of collected holes relative to electrons could be determined. For the three textured samples studied, there indeed appeared to be a good correlation between the n/p collection ratios determined in this fashion and the cell conversion efficiencies. However, a much larger number of samples will need to be examined in this fashion before taking this result too seriously.

In Section 3.1 we acknowledged that we had received an earlier series of nc-Si:H sample devices from United Solar (see Table III). However, corresponding measurements on this earlier series of samples were not very easy to carry out. We believe the reason was that these samples were too thin for our measurement methods; less than 0.9 microns based upon the capacitance freeze-out values. In contrast, the second series of samples appeared to be at least 1.3 microns thick based upon their capacitance freeze-out values. Moreover, the defect densities in these both current series of United Solar samples were much lower than those provided to us previously. This meant that many of our measurements had to be extended into forward bias to avoid depleting the entire i-layer of these devices in many cases.

In Fig. 9 we present our best set of TPC spectra obtained from the earlier set of nc-Si:H samples. These were obtained for MVHF device 2B10514, which was deposited onto specular stainless steel. As with our reported TPC spectra on the previous series of nc-Si:H devices, we observe a decrease in TPC signal above the Si bandgap as the measurement temperature is increased. This is due to an increasing fraction of hole collection with increasing temperature. Indeed, at 325K it appears that only the defect portion of the spectrum remains visible. We also

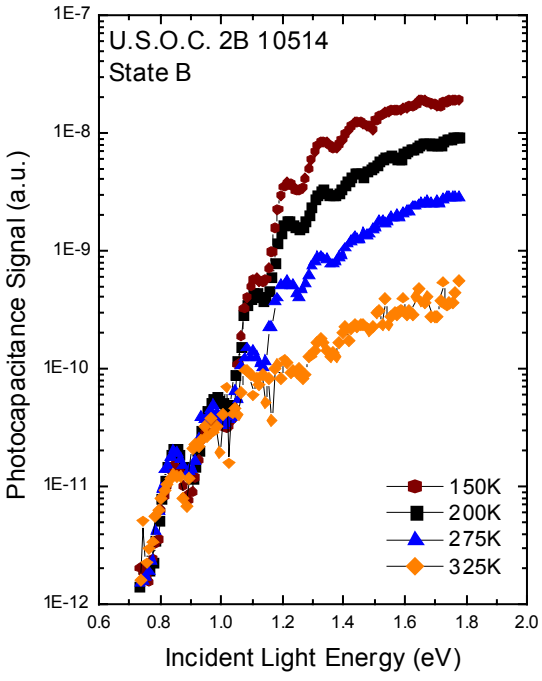

FIG. 9. Photocapacitance spectra for nc-Si:H sample device 2B10514 in its light degraded state. Spectra were taken at 1.1kHz with the ambient reverse bias at –0.2volts and filling pulse height of 0.3volts (to +0.1volts). The signal magnitude decreases above the Si bandgap with increasing temperature due to the increasing fraction of holes collected. The defect band signal is nearly temperature independent and much larger in magnitude than for the previous series of United Solar nc-Si:H samples studied. This is probably due to an insufficient thickness of the i-layer in these sample devices, so that the spectra are dominated by the properties of the material near the back contact; that is, in the n^+ region of the sample device.

observed that the hole collection fraction was significantly better for the annealed state spectra (not shown) compared to those taken after prolonged light exposure. However, in contrast to those earlier reported spectra we did not observe an a-Si:H component to these spectra at higher measurement temperatures. Also, the defect portion of the spectrum is nearly 100 times larger than for those observed in the previous series of samples.

We believe that these differences arise from the insufficient thickness of the i-layer since, during the capacitance transient, the edge of the depletion region actually will expand beyond its position under ambient reverse bias. Because these i-layers are already nearly completely depleted under small values of reverse bias, this means that the edge of the depletion region extends into the n^+ layer near the back contact after the filling pulse and during the transient. Moreover, the region near the edge of the depletion region contributes more strongly to TPC signals than the interior region. This means that the spectra shown in Fig. 9 are probably dominated by the n^+ nc-Si:H layer near the substrate contact. This would account both for the larger defect magnitude and the absence of visible a-Si:H component.

4.2 LIGHT-INDUCED DEGRADATION IN NANOCRYSTALLINE SILICON

Although nc-Si:H does not suffer as severely from light exposure as amorphous silicon, prolonged light soaking typically reduces the conversion efficiency by several percent [12]. Several of our samples were examined both in “State A”, after a sample had been annealed for one hour at 450 K, as well as in “State B”, a degraded state which we obtained by exposing the sample to 20 hours of red-filtered light (>620 nm) from a tungsten-halogen source at an intensity of 400 mW/cm^2. Effects of such light soaking could be observed both in the photo-transient spectra as well as in drive-level capacitance profiles (DLCP). The effect of light soaking on the TPC spectra of sample 13993 is shown if Fig. 10. We see that the TPC signal changes significantly. In particular, the negative signals near 1.5 eV become significantly positive in State B. This corresponds to a loss of hole collection, even more than was achieved by reducing the measurement temperature from 295 K to 275 K in State A (see Fig 7).

In numerous previous studies of light-induced degradation in a-Si:H, DLCP measurements always clearly revealed a systematic increase in the density of deep defects, by factors varying from roughly 2 to almost 50.[13,14] However, our previous DLCP studies for nanocrystalline materials indicated almost no change.[15] and, moreover, very little evidence for a deep defect thermal response at all. In contrast, for some of the current series of nc-Si:H devices, particularly for samples 13993 and 14036, the DLCP measurements have revealed a significant deep defect response, as is illustrated in Fig. 11. This may partly be due to the smaller effective doping levels in these samples which allow us to more clearly observe the contribution from the

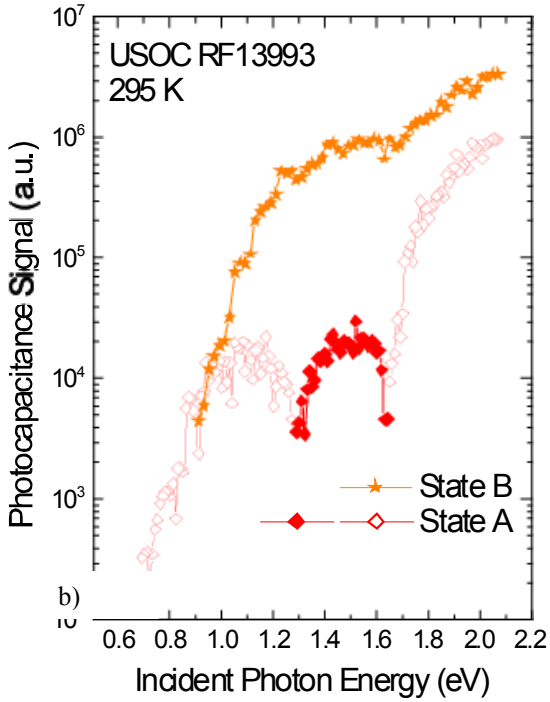

FIG 10. Comparison of the 295K TPC spectra for sample 13993 before after light-soaking. We see an dramatic increase in the magnitude of the TPC spectrum, especially in the regime where the annealed state had exhibited a negative TPC signal. This is due to a substantial reduction in the minority carrier collection.

deep defects. What is even more surprising, however, is that when such a deep defect response is apparent, we consistently find that it *decreases* after prolonged light exposure, as illustrated in Fig. 11b.

To explain the observed effects of light-soaking on the DLCP and TPC measurements, we tentatively propose a microscopic degradation model. First, we note that that DLCP density represents the integral over the density of states in the gap between the Fermi level and a thermal response energy. Thus, the observed decrease in drive level density may result from defects

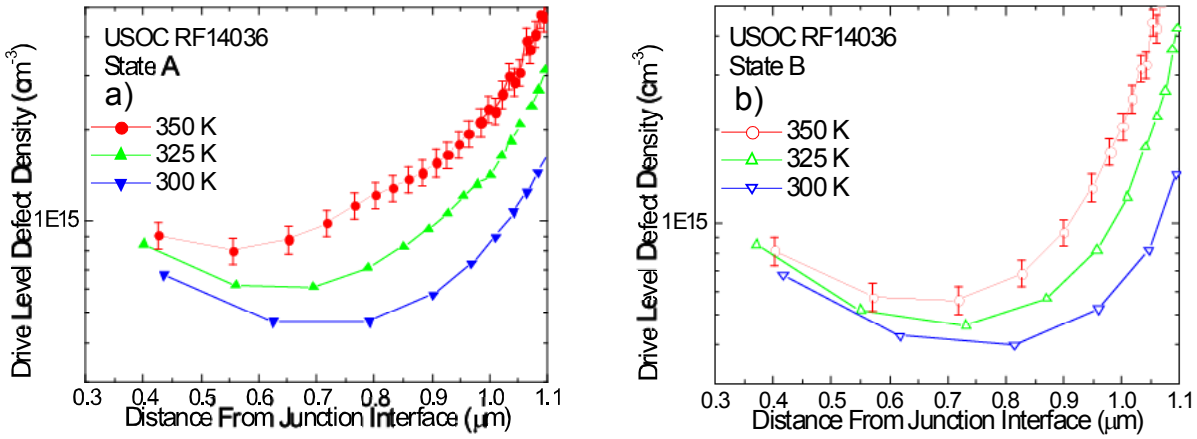

FIG 11. 1.1 kHz DLCP profiles obtained for a series of temperatures for both (a) the annealed State A and (b) light-soaked State B of one nc-Si:H sample deposited on specular stainless steel. The increasing density with temperature is due to the response of deep defects. However, this response from the deep defects actually appears to be reduced after light soaking. Representative errors are shown in for the 350K spectrum in each case.

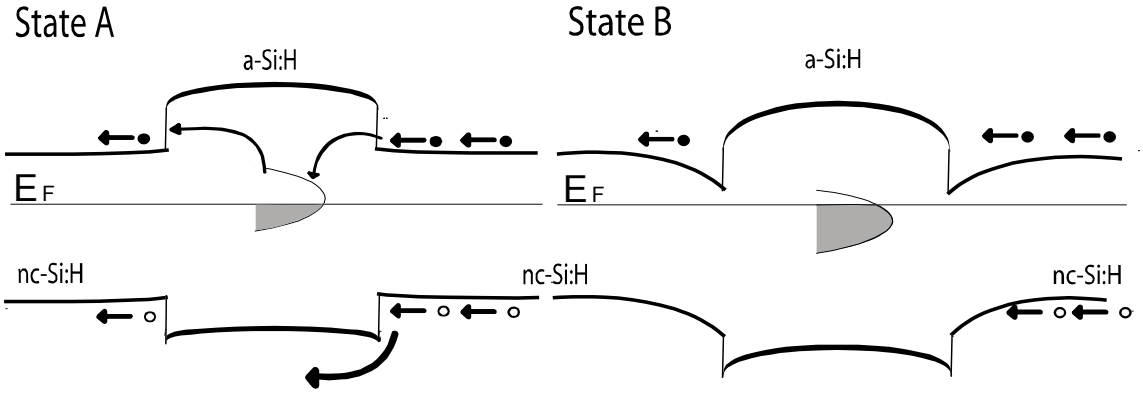

FIG 12. Schematic of a possible model to explain light-induced changes observed in the drive-level profiles and the photocapacitance spectra of nc-Si:H. In State B, defects have shifted down in energy with respect to the bulk conduction band and holes see a larger potential barrier at the phase boundary. In the scenario illustrated, positive charge has collected at the a-Si:H/crystallite interfaces, and is compensated by negative charge in the a-Si:H region, as well as in the crystallite nearby.

effectively "shifting out" of the energy region defined by our DLCP measurement parameters. At the same time, the observed reduced hole-collection implies an impediment to hole transport. Both of these observed effects could result from of a shift in the potential distribution between the nanocrystallites and amorphous regions of these mixed phase materials, as shown in Fig. 12. Such a shift in the relative potentials of the two phases might occur during light-soaking by a separation of the photo-generated charges, with positive charge accumulating at the amorphous-nanocrystalline phase boundary, and compensating negative charge being added to the dangling bond defects within the amorphous regions. Studies have already begun to test some of the other possible implications of such a microscopic model.

5.0 NREL HOT-WIRE AMORPHOUS SILICON-GERMANIUM ALLOYS

5.1 REVIEW OF PREVIOUS WORK

Last year we reported that a-Si,Ge:H alloys grown by the hot-wire chemical vapor deposition (HWCVD) method could exhibit electronic properties as good as the best glow discharge (PECVD) a-Si,Ge:H alloy films.[16,17] This resulted from replacing the usual tungsten filament with tantalum and using a filament temperature of ~1800°C instead of ~2000°C. For HWCVD a-Si,Ge:H alloy films deposited in this fashion with Ge fractions in the 15 to 50 at.% range (Tauc gaps were between 1.65eV to 1.3eV), Urbach energies were found to lie below 45 meV. In addition, for Ge fractions up to 30 at.%, the annealed state deep defect densities were found to lie at or below the mid $10^{15}cm^{-3}$ level.[17] These recent HWCVD grown alloys also exhibited roughly an order of magnitude lower structural defect density as measured by small angle X-ray scattering (SAXS) studies for Ge fractions ranging from 20% to as high as

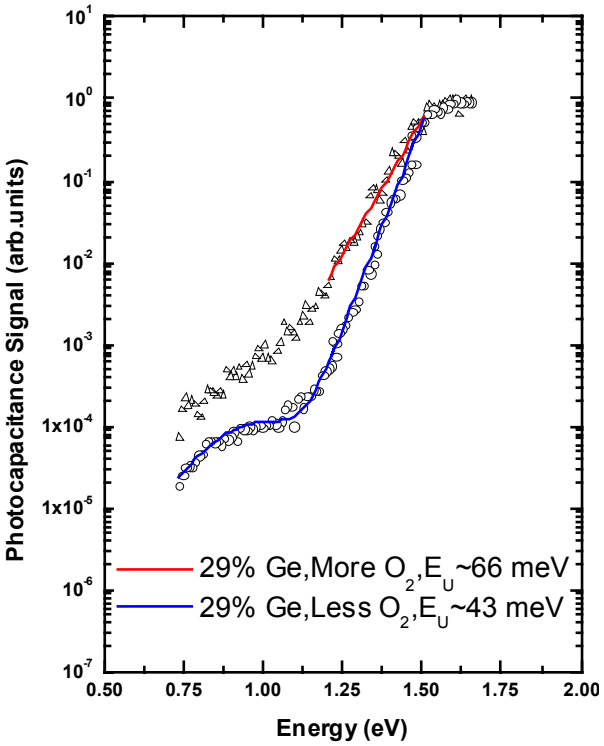

FIG. 13. Comparison of TPC spectra on two 29at.% Ge films, with the later film exhibiting poorer electronic properties evidence by broader bandtail and larger defect band.

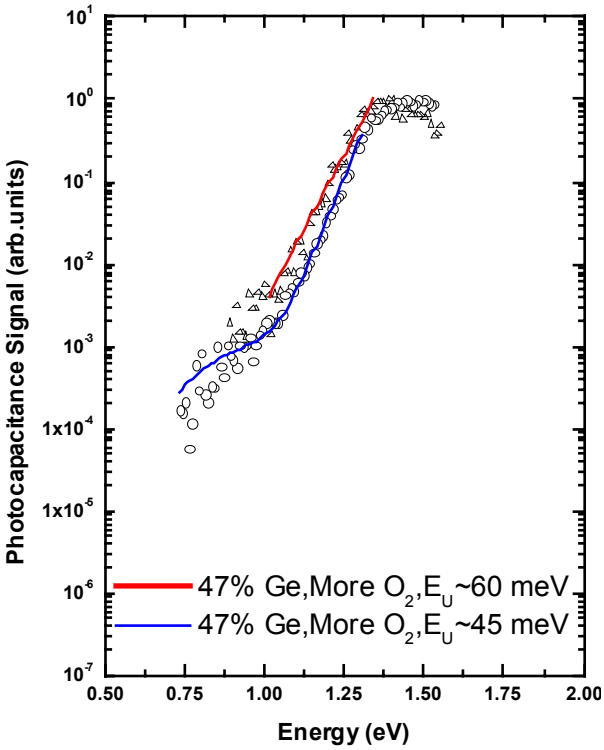

FIG. 14. Comparison of TPC spectra on two 47at.% Ge films, with the later deposited film again exhibiting poorer electronic properties.

80% compared to all past a-Si,Ge:H thin films grown by either by PECVD or HWCVD. [16,18,19] Moreover, because these HWCVD a-Si,Ge:H alloys could be deposited at substantially growth rates than the best PECVD a-Si,Ge:H films, this method potentially might greatly impact the future development of amorphous Si based photovoltaic technology.

5.2 EFFECTS OF OXYGEN CONTAMINATION

Shortly after determining that the HWCVD deposited a-Si,Ge:H alloys exhibited such seemingly good electronic properties, we learned that series of such films deposited subsequently at NREL did not appear to exhibit such good properties. We were provided with a couple of these more recent a-Si,Ge:H samples and indeed found, in late Spring 2005, that these films had inferior properties to those we had previously examined. In Fig 13, we display a comparison of the TPC spectra of two 29at.% Ge samples, the initial film that exhibited very good properties (Sample 1306) and the later film (1430) with much poorer electronic properties. A similar result was obtained for two 47at.% Ge samples (1307 and 1431) shown in Fig. 14. The poorer electronic properties in the later films are clearly evidence by broader Urbach tails and a defect band with a larger magnitude in both pairs of samples.

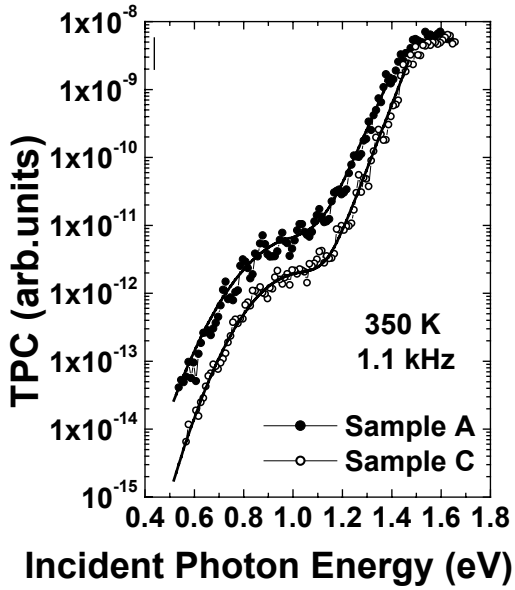

FIG. 15. TPC spectra of a-Si,Ge:H sample A (no intentional air leak) and sample C (with a 0.06 sccm air flow during growth). Solid lines represent detailed numerical fits to these spectra.

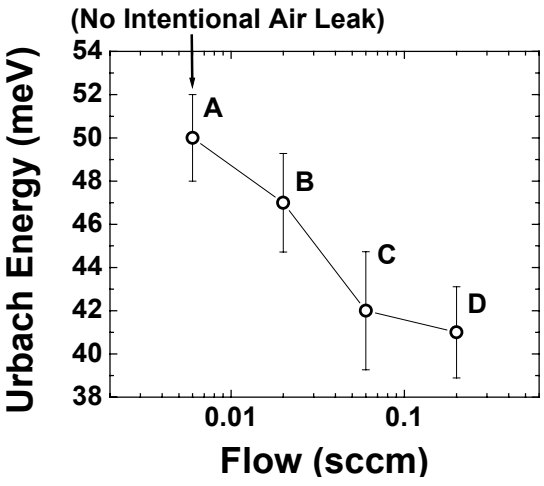

FIG. 16. Urbach energies obtained from the detailed fits of the four controlled air-leak HWCVD a-Si,Ge:H samples.

Our DLCP measurements also indicated nearly an order of magnitude larger deep defect density for the 29at.% a-Si,Ge:H (at roughly $2.6\pm0.25 \times 10^{16}$ cm^{-3}) compared to the earlier 29at.% sample. Subsequent SIMS analysis determined that the later samples contained significantly higher oxygen levels due to a contaminated GeH_4 gas line. It thus seemed plausible that the higher level of oxygen impurities had been responsible for the poorer electronic properties. This apparent sensitivity to oxygen impurities was, however, very surprising because similar levels of oxygen have not been found to appreciably affect the properties of a-Si:H. [20]

The source of oxygen contamination during the HWCVD growth process was identified and eliminated in the Fall, 2005. We then decided it would be interesting to understand to what extent controlled changes in the level of oxygen contamination would affect the electronic properties of these samples. Therefore, a series of four a-Si,Ge:H alloy samples were deposited using a controlled leak valve to introduce a systematic variation in oxygen level during the HWCVD process. Oxygen levels varied from less than 1×10^{19} cm^{-3}, with no intentional air leak, to about 5×10^{20} cm^{-3}, when the air-leak was at 0.2 sccm (see Fig. 1 in Section 2). All of these a-Si,Ge:H films were deposited simultaneously on stainless steel and p^+ c-Si substrates.

In Fig. 15 we display the TPC spectra of the sample grown with no intentional air-leak and one with a 0.06 sccm air flow, both on stainless steel substrates. It appears that the increased oxygen content of second sample in this case actually resulted in a film with a narrower bandtail and a reduced deep defect band as compared to the zero air-leak sample. The spectra are well

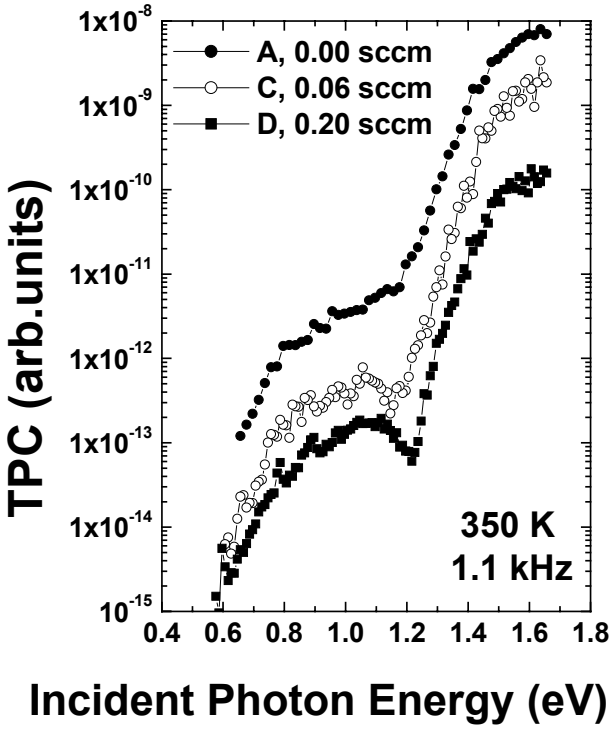

FIG 17. TPC spectra for 3 of the HWCVD a-Si,Ge:H films co-deposited onto the p^+ c-Si substrates. These curves have been vertically offset for display purposes. The Urbach energies for samples A, C, and D were determined to be 43, 38, and 45 meV, respectively.

fitted assuming an exponential band tail along with a single gaussian band of deep defects. In Fig. 16 we plot the deduced Urbach energies of all four of a-Si,Ge:H films deposited on the stainless steel substrates. This figure again indicates that increasing oxygen levels actually *improve* the quality of these alloy films. In Fig. 17 we display TPC spectra for three of the films that were co-deposited onto the c-Si substrates. Here we find an Urbach energy slightly below 40meV for the 0.06sccm air-leak sample, one of the narrowest ever obtained in a-Si,Ge:H alloy films. In this case, however, a slight increase in E_U is observed for the sample deposited with the highest oxygen.

Given that the a-Si,Ge:H films were *co-deposited* onto the stainless-steel and c-Si substrates, the reason for the differences in the electronic properties on the two types of substrates revealed by these sub-band-gap spectra seems difficult to understand. An important aspect may be that the measurements on the stainless-steel substrate samples were made utilizing the top Schottky contact, while for the c-Si substrate samples the bottom p^+n junction was used. Because the substrate temperature increased substantially during deposition (Table IV), the differences in properties may thus reflect these variations in the growth temperature.

In several previous studies of a-Si,Ge:H alloys, a direct relationship was established between the Urbach energies deduced by such sub-band-gap spectra and the deep defect densities determined by DLCP measurements.[21] This relationship agrees with the spontaneous bond breaking model which predicts a lower deep defect density for samples exhibiting smaller

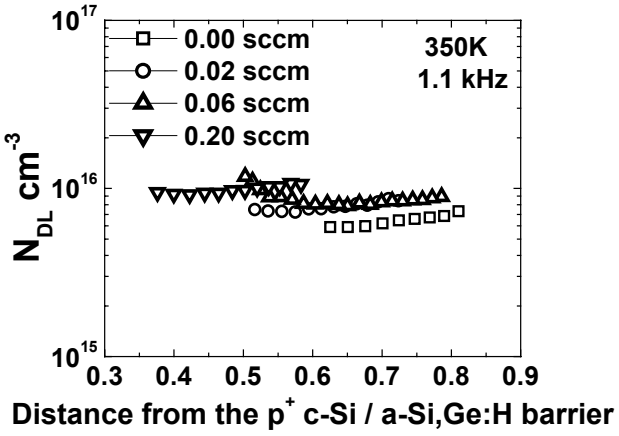

FIG. 18. DLCP deep defect density profiles of the a-Si,Ge:H films deposited onto the p^+ c-Si substrates. Note the general increase in density with higher air-leak. This may indicate a small degree of n-type doping with increasing oxygen.

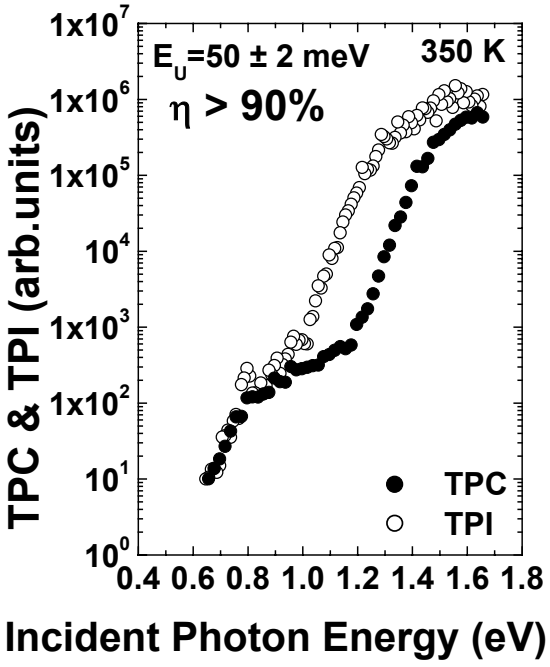

FIG. 19. Comparison of TPC and TPI spectra for the film deposited onto the c-Si substrate at zero air-leak .

Urbach energies.[22] In Fig. 18 we plot the defect density determined by the DLCP technique for the films deposited onto the crystalline Si substrates. Somewhat surprisingly, we observe that the DLCP density actually increases as the oxygen content of the samples are increased. This observation may be reconciled with the predictions of the spontaneous bond breaking model if we assume that oxygen not only improves the quality of the a-Si,Ge:H alloys but also acts as a weak donor since, in that case, the neutral bulk Fermi level would be shifted upward, thus increasing the contribution of the defect density determined by DLCP. Further experiments will soon be conducted to verify this hypothesis.

Finally, to obtain an estimate of the relative degree of minority carrier collection, we compared the TPC and TPI spectra for the a-Si,Ge:H deposited onto the c-Si substrate. This provides us with the *sum* of the electron and hole photogenerated carriers that escape the depletion region in the measurement time window (in the TPI spectrum), as well as the *difference* (in the TPC case). In such measurements of the best PECVD samples, we have determined relative hole collection that exceeds 95%.[23] Previously, the best such value determined for the HWCVD deposited alloy samples was roughly 75%.[24] However, for the spectra displayed in Fig. 19 for the a-Si,Ge:H deposited without an intentional air leak but with a higher oxygen level than that previously reported [24], we obtain a value that exceeds 90%. This result thus clearly underscores the high quality of these HWCVD a-Si,Ge:H alloys.

5.3 LIGHT-INDUCED DEGRADATION IN HWCVD a-Si,Ge:H

We continued our studies of light-induced defect creation in these HWCVD deposited a-Si,Ge:H that we began last year. We employed DLCP measurements to examine the defect creation and annealing kinetics of one of the HWCVD grown samples (1306) with a 29at.% Ge fraction. To help identify specifically the aspects of degradation that are unique to the HWCVD deposited alloys, we have compared the behavior of this sample to that of a PECVD grown 35at.% Ge sample with a similar optical gap (near 1.5eV) that we had obtained several years ago from United Solar. In both cases we used a tungsten-halogen light source filtered with a 610 nm long pass filter at a net intensity of roughly 800 mW/cm^2 (after correcting for absorption in Pd top contact). During exposure the sample temperatures were maintained below 330K. After each consecutive period of light soaking the defect densities were determined by carrying out DLCP at 360 K and 1100 Hz. Figure 20 displays one full set of spatial profiles obtained in this fashion at 1.1 kHz for a-Si,Ge:H sample 1306.

In Fig. 21(a) we display on log-log axes the spatial average of the relatively flat portion of these DLCP profiles to obtain the characteristic defect density as a function of *accumulated* light soaking time for the HWCVD and PECVD a-Si,Ge:H alloys of 1.5eV optical gaps. Densities of deep defects for both samples have been normalized to their respective initial State A values. The defect density for the HWCVD sample rises slowly for the first 3 minutes of light soaking, reaches a relatively constant plateau, and then subsequently increases much more rapidly after about 1.5 hours of light soaking. For the PECVD sample, the light induced defects exhibit an initial slow rise and then also show a much more rapid increase (beyond roughly the ½ hour mark). A plateau region is not so distinct for this sample, while the final rate of increase of defect density beyond 4.5 hours is actually higher for the PECVD sample than that of HWCVD sample. The long time regime exhibits roughly a power law dependence for both samples (with

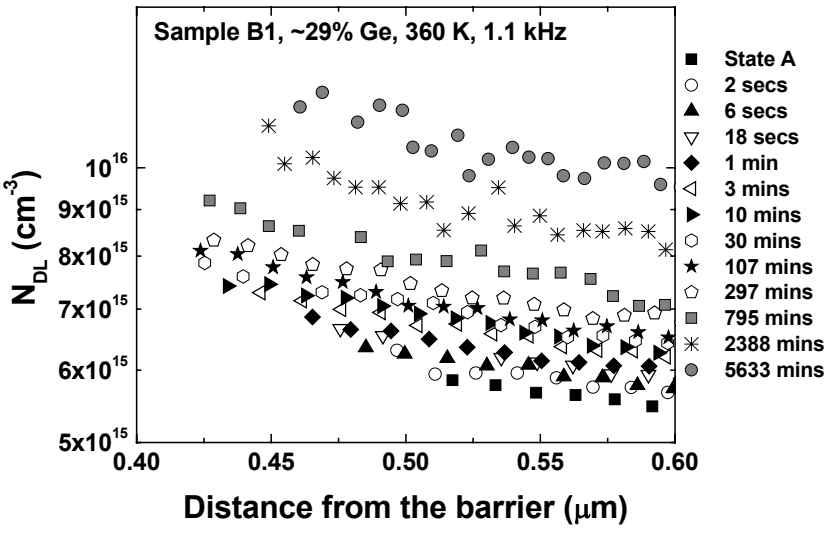

FIG 20. Example of DLCP profiles for the 29at.% Ge alloy Sample 1306 at different stages of light induced degradation. Spatial averages of N_{DL} were obtained around 0.55 μm to construct the time evolution of defect density shown for this sample in Fig. 21

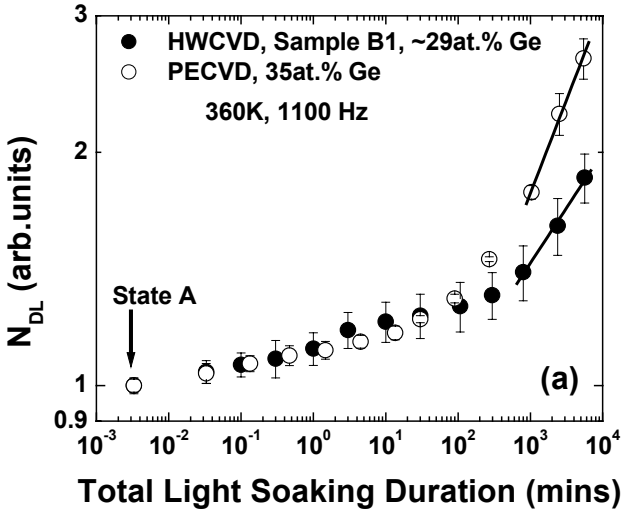

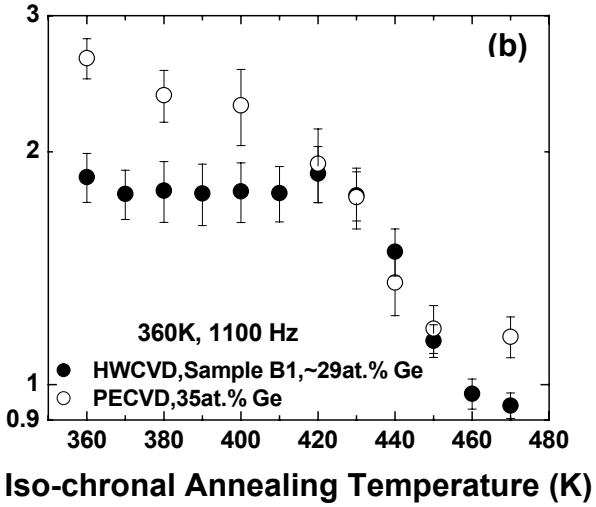

FIG. 21(a). Time evolution of defect densities during light soaking for 29at.% Ge HWCVD Sample 1306 and for a 35at.% Ge United Solar PECVD alloy sample. These data have been normalized to the initial State A values: 5.7×10^{15} cm^{-3} and 2.5×10^{15} cm^{-3}, respectively.

(b). Decrease of deep defect densities as a result of a series of 10 minute isochronal anneals at increasing temperatures as indicated. Note that the HWCVD sample exhibits a much narrower range of energy activation barriers for thermal annealing .

exponents of 0.24 ± 0.014 and 0.14 ± 0.012 for the PECVD and HWCVD samples, respectively).

The annealing kinetics for the two samples are compared in Fig. 21(b). In both cases we employed a series of 10 minute isochronal anneals beginning at 360K, and increasing in 10K steps up to final anneal at 470K. The same conditions were employed for determining the defect densities from the DLCP measurements (360K at 1100Hz), and the defect densities remain normalized to their *initial* State A values.

For the PECVD a-Si,Ge:H one observes that the defect density decreases slowly but monotonically, ultimately reaching its initial State A density after the 470K anneal within experimental error. This is distinctly different than the behavior of the HWCVD grown sample which anneals within a much smaller temperature range. This seems to indicate a much narrower range of annealing energy barriers for this HWCVD sample. However, at temperatures higher than 430 K the annealing rates appear nearly same for both the samples.

6.0 STUDIES OF COPPER INDIUM-GALLIUM DISELENIDE SOLAR CELLS

For the CIGS portion of work supported this Subcontract we were to apply our measurement techniques to try to understand differences between the best laboratory cells, and those fabricated using processes better suited for manufacturing. For this Subcontract year we are reporting what we have learned from a set of high performance NREL CIGS devices that were obtained in 2005 from Miguel Contreras (see Table V, Section 2.3).

6.1 BACKGROUND

Some of earliest studies used to examine the electronic properties of the CIGS absorber within a solar cell device employed admittance spectroscopy, typically displayed in the form of capacitance vs. temperature and frequency. Quite typical results are shown for a sample from the Institute of Energy Conversion, University of Delaware in Fig. 22. These capacitance curves are plotted vs. *descending* temperature to allow a more direct comparison with the capacitance vs. log(frequency) plots on the NREL devices shown later. These curves merge at the lowest temperatures to the depletion width capacitance (εA/W), and then exhibit a step increase before reaching another plateau at the highest temperatures displayed. This step increase arises from the well-known "deep acceptor" band, which usually is the dominant majority carrier trap in the CIGS absorber layer. The step shows a thermally activated signature in an Arrhenius plot. Such behavior has been observed in CIGS devices fabricated from a large number of sources.[25]

Initially there had been some uncertainty whether this admittance step was due to a "bulk" defect distributed throughout the CIGS layer or whether it existed only in the vicinity of the barrier interface.[4] In Fig. 23 we have employed DLCP measurement to spatially profile "energy slices" of the states that are able to respond at the different measurement frequencies at a temperature of 165K. The profiles shown in Fig. 23(a) clearly indicate that the capacitance step in Fig. 22(a) is due to a bulk defect fairly uniformly distributed throughout most of the CIGS layer. In Fig. 23(b) we have extended these DLCP profiles considerably into forward bias to

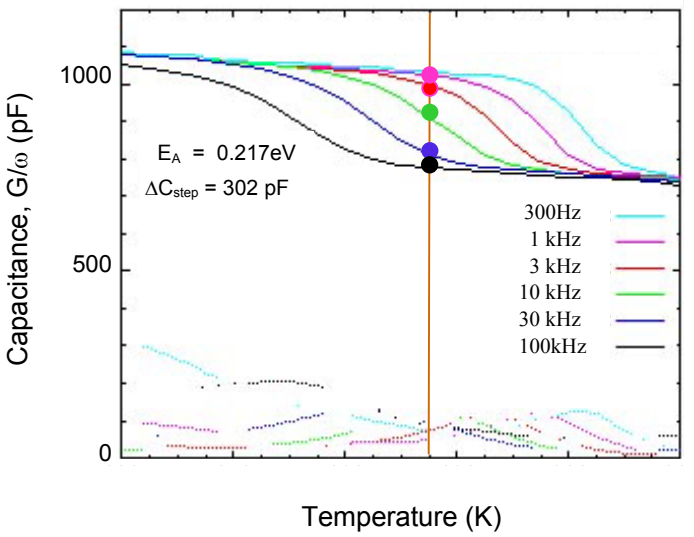

FIG. 22(a). Capacitance vs. temperature at 6 measurement frequencies for an IEC CIGS device at zero bias. The distinct temperature step corresponds to a bulk "deep acceptor" defect. The vertical line at 165K and solid circles indicate the conditions under which drive-level capacitance profiling measurements were carried out. These are displayed in Fig. 23.

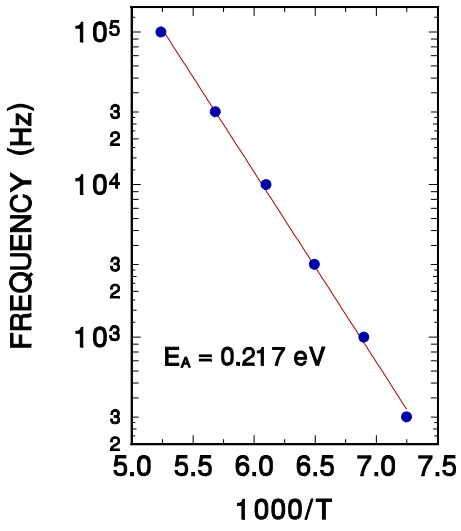

(b). Arrhenius plot of inflection points at center of step obtained from the capacitance vs. temperature curves of Fig. 22(a). The activation energy indicates a majority carrier (hole) trap lying roughly 0.22eV above E_V.

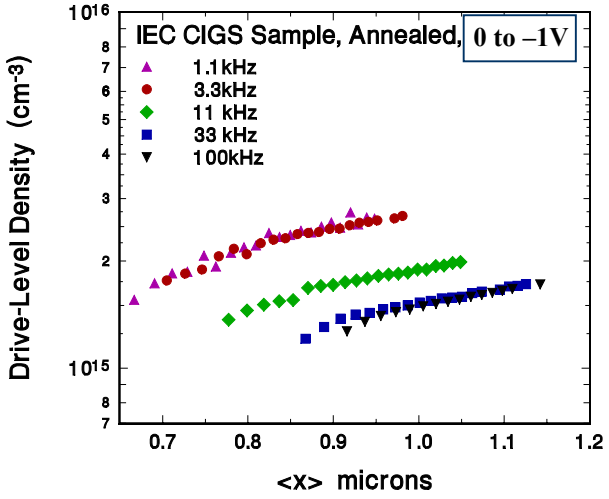

FIG. 23(a). Drive-level capacitance profiles taken near 165K at 5 measurement frequencies. The limiting value at the highest frequencies, near 1.5 x 10^{15} cm^{-3}, indicates the free (hole) carrier density, while the limiting value at the lowest frequencies indicates the *sum* of free carriers plus deep acceptors. This implies a deep acceptor density of roughly 1.2 x $10^{15}$$cm^{-3}$.

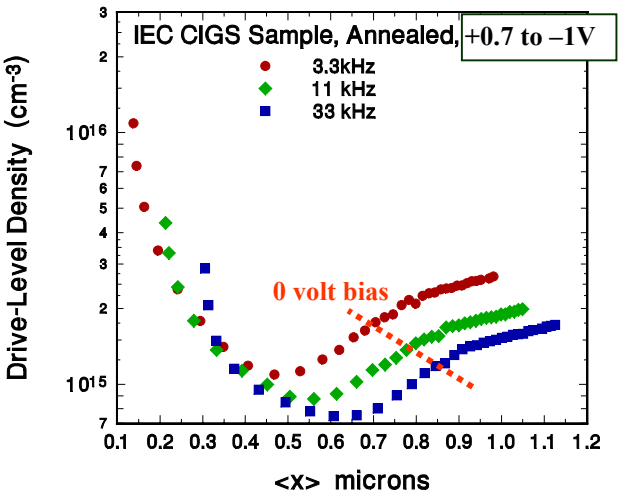

(b). Extended DLCP curves obtained by extending the range of DC bias to 0.7volts forward. This allows a region much closer to the barrier interface to be examined compared to Fig. 22(a); specifically, the region to the left of the red dashed line. Clearly, the electronic properties of the CIGS layer vary substantially close to the barrier.

examine the electronic properties much closer to the barrier interface. Here we observe a much more pronounced spatial variation which seems to indicate very different electronic properties in this region of the CIGS layer. Since this is the spatial region that dominates the collection of photo-generated carriers in the working device, understanding the electronic properties in this region are probably much more important than those in the normally undepleted portion of the CIGS layer.

A multi-investigator collaboration of the NREL Thin-Film Partnership CIGS Team was recently published [25] which concluded in part that there was a strong inverse correlation between the CIGS cell performance and the magnitude of this deep acceptor capacitance step. This conclusion was based upon admittance measurements CIGS devices from six different laboratories. However, these measurements, performed under zero applied bias, probably did not probe the defect properties closest to the barrier interface, such as those revealed at profiling distances smaller than about 0.6μm in Fig. 23(b).

6.2 RESULTS ON NREL CIGS CELLS FROM ADMITTANCE MEASUREMENTS

The results of admittance measurements on the NREL sample devices we examined are generally consistent with the finding that CIGS devices with the highest efficiencies generally do not show a deep acceptor step-like feature like those in Fig. 21(a). Representative examples of

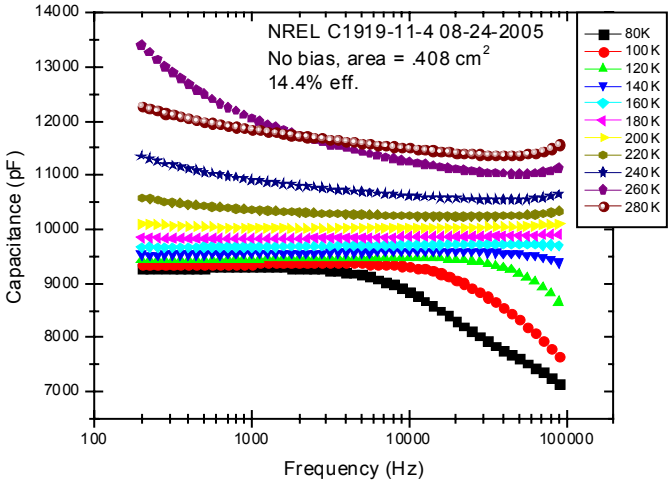

FIG. 24. Capacitance vs. frequency at zero bias for one device from each of the 3 sample depositions. The spectra from neither the C1813-21 device nor the C1924-1 device exhibit the typical admittance step due the response from the deep acceptor level observed in devices from most other laboratories. The low temperature falloff at high frequency for these two devices is believed to be a measurement artifact (see discussion in text). The depletion capacitance varies slightly from sample to sample, but does not correlate in any obvious manner to the device cell performance.

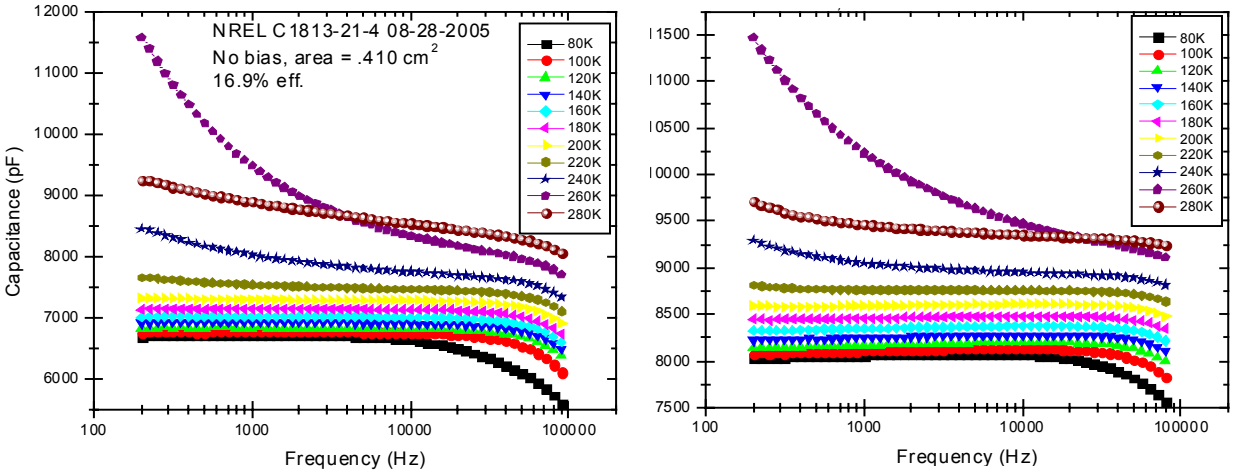

capacitance vs. frequency data for on sample device from each of the three depositions are displayed in Fig. 24. Except possibly for the C1919-11 device, these devices show very little evidence for the admittance step typical of devices from other laboratories. There does appear to be a roll-off at the very highest frequencies for the other 2 devices; however, this does not correspond to the deep acceptor admittance feature that is normally seen. Rather, this roll-off is more likely due either to impedance problems with our current preamplifier or, possibly, due to the limited conductance of the window layer. Both issues arise because these devices have much larger areas than those we have measured in the past. For example, a limited sheet conductance would reduce the effective area of the sample at higher frequencies and low temperatures and produce the type of decrease in capacitance that is observed.

In spite of the lack of such a deep acceptor feature in the admittance spectra of these NREL CIGS devices, and the lack of even any major differences in the junction capacitances, the efficiencies of the devices do vary considerably, as seen in Table V in Section 2.3. However, much more pronounced differences are revealed from our DLCP profiling measurements discussed below.

6.3 CAPACITANCE PROFILING RESULTS

In Figure 25 we display results of both DLCP and standard CV profiling for these same 3 representative sample devices. The sample bias was varied from 1 volt reverse to +0.4 volts

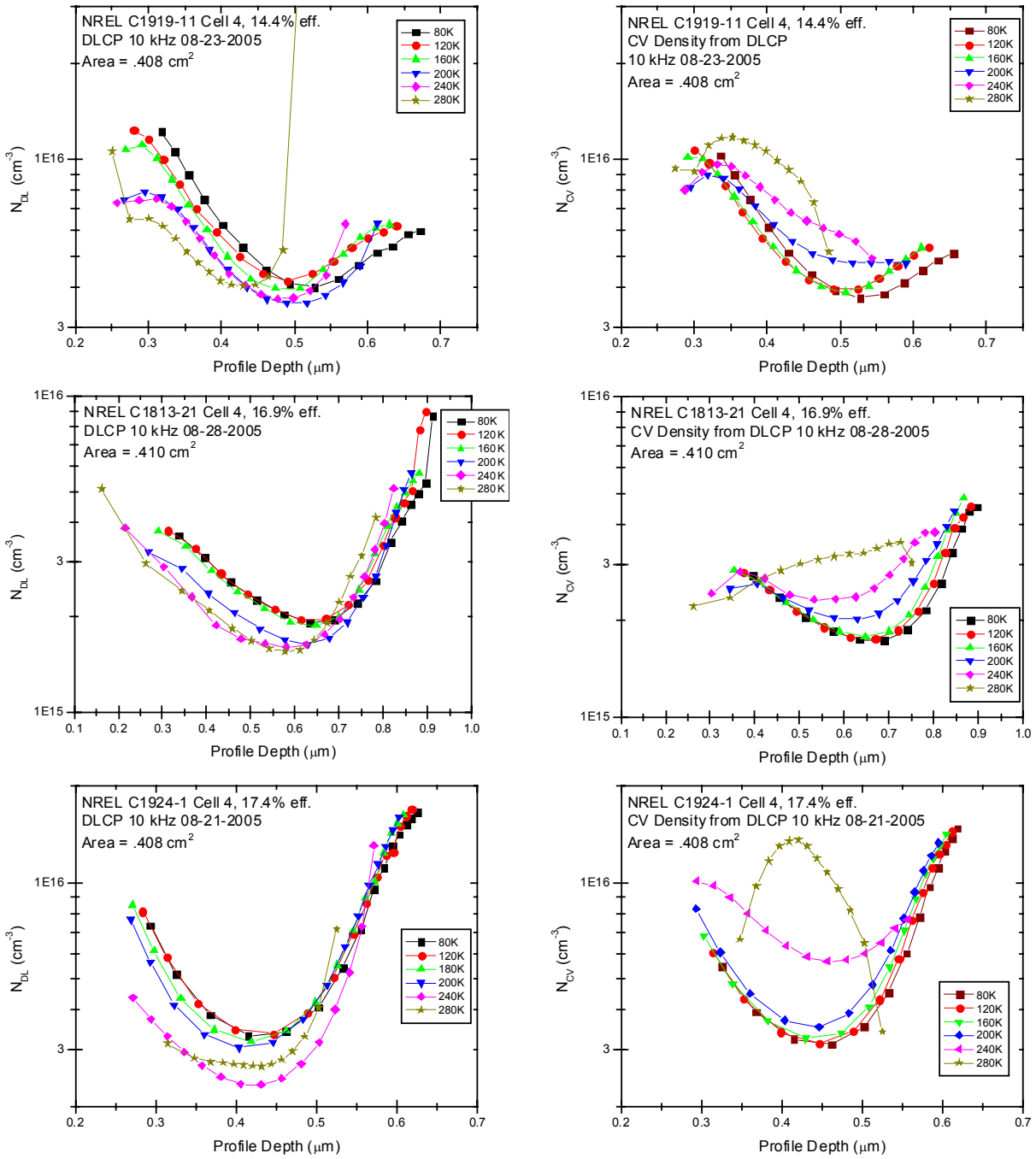

FIG. 25. Drive-level capacitance profiles (DLCP) and CV profiles for representative devices over a broad range of temperatures. These data were taken using DC biases that varied from –1V to +0.4V, in 0.1V increments. Note the strong spatial variation in these profiles in all cases. Also note the similarity between the DLCP and CV profiles for temperatures of 160K and below, but the marked differences for the highest temperatures employed.

forward and, in all cases, we observe quite a pronounced spatial variation in these profiles. The temperature dependence is quite interesting: For temperatures below about 160K the profiles are nearly temperature independent, and the differences between the DLCP and CV curves are very minor. This changes for the profiles obtained at 200K and above. Indeed, for the 280K profiles, the differences between the DLCP and CV profiles become quite pronounced, with the latter showing a dramatic peak in some cases.

Because of the observed large spatial variations in these profiles, the usual simple interpretation of DLCP in terms of the expression given by Eq. (2) in Section 3.3 may not be very accurate. However, we have recently enhanced some of our numerical modeling programs so that we can extract more detailed information from the types of DLCP and CV profiles shown. This analysis has just begun, however, so that we cannot present results from our more accurate analysis in this Report.

Nonetheless, we can offer some general conclusions at this time. First of all, the large CV profile densities at high temperature are almost certainly due to very deep defects near the barrier interface (even though they occur for profile "distances" that appear to be at some distance from the barrier). In this case, a clearer picture of the distribution of these deep, near interface states must await a more detailed numerical modeling analysis. For this reason we will concentrate our remaining comments on our DLCP results. Clearly, the appearance of the DLCP profiles is qualitatively different for the different representative samples. For the C1919 (lowest performance) device, the DLCP profile is high in the region near the barrier interface (obtained under forward bias so that this region lies in the high field region under normal operation), and relatively low at larger distances from the barrier (this is the region that lies outside the depletion region in nearly zero field). For the other two, higher performance devices the DLCP density is relatively lower in the normally depleted region close to the barrier, and relatively higher in the zero-field region at larger distances.

To get a better idea of how our DLCP results might be correlated with the device performance, we have plotted in Figure 26 how the device efficiencies vary with the DLCP densities in the normally depleted region of the device closer to the barrier interface [Fig. 26(a)] and also with the DLCP density in the normally zero-field region of the absorber farther away from the barrier interface [Fig. 26(b)]. From Fig. 26(a) we see that, for the 5 devices from two of the depositions, there appears to be quite a good inverse correlation between the cell efficiencies and the DLCP densities close to the barrier interface. It is thus tempting to connect the larger DLCP densities in the depletion region of these devices with a larger concentration of recombination centers that lower the fill factor, and hence the efficiencies. On the other hand, the cells from the third, C1924-1, deposition do not follow this trend. However, we believe that this might be the result of our inaccurate interpretation of these DLCP profiles since, for the

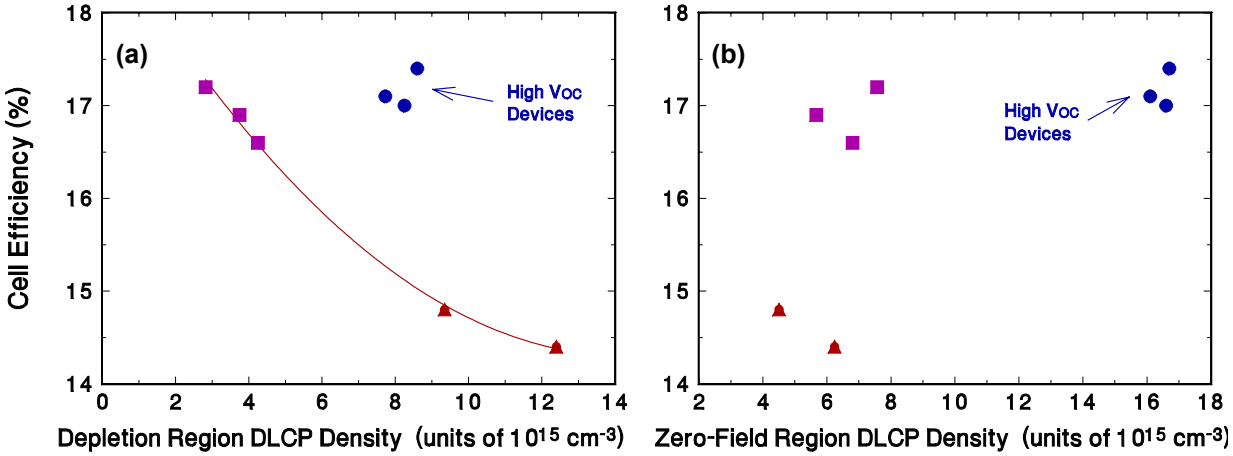

FIG. 26. Correlation of device efficiencies with the DLCP determined densities in the: **(a)** depletion region near the barrier interface, and **(b)** the zero field region of the absorber farther from the barrier interface. The symbols are used in the same manner as in Figs. 1 and 2; namely: ▲ for the C1919 devices, ■ for the C1813 devices, and ● for the C1924 devices. These latter devices were found to have significantly higher values of V_{OC} than the others, and are so labeled.

C1924 devices (see Fig. 25), they exhibit the largest spatial variations and thus may be less likely to reflect the true spatial distributions in the electronic properties. Indeed, we note that some of our recent modeling has indicated that the type of large upturn in the DLCP profiles that are exhibited for the C1924 devices at forward bias probably reflect characteristics of the barrier interface itself, rather than defects within the absorber. In contrast, the DLCP curves for the C1919 and C1813 devices appear show signs of flattening out at small profile distances. In some of our attempts to model similar kinds profiles in more detail, we have found that they usually reflect the actual defect densities within the absorber layer close to the barrier interface.

Fig. 26(b) indicates that the high V_{OC} devices are also distinctive in displaying much higher DLCP densities in the zero-field region outside the depleted part of the absorber. This is undoubtedly beneficial for the device performance for two reasons: (1) It means that the hole carrier density is higher in this region, leading to a lower resistivity within the part of the absorber less active in power generation, and (2) The higher DLCP density reflects a hole carrier density that is higher by a factor of 2.5 to 4 times that of the five less efficient devices. This means that the hole Fermi level near the back contact is probably 25-35 meV closer to E_V, and this will be reflected in a higher value of V_{OC}. We believe that this could account for about half of the difference in V_{OC} for the C1924-1 devices compared to the other devices. The remainder of the difference in V_{OC}, we believe, likely comes from differences in the composition profiles of the C1924-1 devices.

7.0 SUMMARY AND PLANS FOR FOLLOW-UP STUDIES

During this first phase of our NREL Subcontract period we have focused on three areas of study. First, we have continued our work to characterize the electronic properties of nc-Si:H materials obtained from United Solar. A number of new sample devices were obtained and, unlike our previous work on nc-Si:H which utilized specialized sandwich structures, all of the samples studied during the past year were actual working n-i-p solar cell devices. The properties of the nc-Si:H layers deduced for these samples were qualitatively identical to those obtained previously from the sandwich-type devices.

Because the nc-Si:H layers in these more recent samples appear to be somewhat more intrinsic than those studied previously, with electron carrier densities estimated to lie below 10^{15} cm^{-3}, we were able to obtain a definite deep defect response in our DLCP measurements for some of the samples. Surprisingly, this defect signal was observed to decrease after light-soaking rather than increase. At the same time, the minority (hole) collection fraction was significantly degraded. This led us to propose a preliminary microscopy model to explain these observations. This model assumes that the relative electron potentials of the amorphous regions are shifted downward as a result of light-soaking, presumably from some type of light-induced charge separation across the phase boundaries of these mixed phase materials. Plans for the immediate future include trying to obtain additional experimental evidence to verify or refute the detailed implications of such a model. We also are planning to examine a larger number of n-i-p sample devices to see if we can correlate the cell performance parameters with the degree of minority carrier collection as revealed by our measurements.

Second, we continued to examine the HWCVD a-Si,Ge:H alloys deposited at NREL by Yueqin Xu. Although the first set of these samples examined in 2004 had revealed very good electronic properties, a couple later samples did not. This was believed to be a result of excess oxygen contamination. Once the source of this contamination was identified at NREL and eliminated, we obtained a series of four samples with varying levels of excess oxygen introduced in a controlled manner using a variable air-leak. Surprisingly, these samples did not show a degradation in electronic properties as a result of increasing oxygen levels. Moreover, the samples with moderate levels of oxygen actually revealed smaller Urbach energies, to below 40meV in one case. On the other hand, the midgap defect level, measured using DLCP, showed a modest increase as the oxygen level was increased.

We tentatively concluded that the modest increase in the midgap defect density was due oxygen acting as a weak donor. This conclusion is now being tested by determining the Fermi level positions in this series of samples using detailed admittance measurements. We have also began examining the kinetics of light-induced degradation and annealing in these samples. It

appears that these kinetics are somewhat different than those obtained in high quality PECVD a-Si,Ge:H films. In particular, the metastable deep defects anneal away over a much narrower ranges of temperatures than the PECVD a-Si,Ge:H films. We plan to extend these degradation studies to the samples with modest oxygen levels in the near future.

Finally, we applied both admittance and DLCP measurements to a set of CIGS photovoltaic devices that were obtained from Miguel Contreras at NREL. The ultimate goal in this work is to identify differences in the electronic properties of the CIGS absorber layer in laboratory produced devices compared to those produced using processes more suitable to large scale manufacturing of CIGS modules. In the case of the NREL cells we examined eight devices that varied in their level of performance, from about 14.4% to nearly 17.5% efficiency.

Admittance measurements carried out at zero volts applied bias did not reveal significant differences among this set of films. However, the DLC profiles did vary significantly. In particular, the DLCP determined defect density obtained under forward bias conditions, probing the defects in the region closest to the barrier interface, seemed to be reasonably well correlated to the device efficiencies over this set of samples. Future work in this area will examine CIGS devices from additional sources, particularly those produced from manufacturing relevant processes. In addition, a more detailed analysis of the DLCP profiles will be carried out using our newly adapted numerical modeling methods. This analysis will hopefully identify more accurate correlations between the electronic properties in these films and the device performance parameters.

8.0 SUBCONTRACT SUPPORTED PUBLICATIONS

1. Adam F. Halverson, James .J. Gutierrez, J.David Cohen, Baojie Yan, Jeffrey Yang, and Subhendu Guha, “Electronic characterization and effects of light-induced degradation on hydrogenated nanocrystalline silicon”, Appl. Phys. Lett. **88**, 071920 (2006).

2. Shouvik Datta, Yueqin Xu, A. H. Mahan, Howard M. Branz, and J. David Cohen, “Superior structural and electronic properties for amorphous silicon-germanium alloys deposited by a low temperature hot wire chemical vapor deposition process”, J. Non-Cryst. Solids, in press.

3. P.G. Hugger, S. Datta, P.T. Erslev, Guozhen Yue, Gautam Ganguly, Baojie Yan, Jeffrey Yang, Subhendu Guha, and J.D. Cohen, “Electronic characterization and light-induced degradation in nc-Si:H solar cells, Mat. Res. Soc. Symp. Proc. **910**, in press.

4. Shouvik Datta, J. David Cohen, Steve Golledge, Yueqin Xu, A. H. Mahan, James R. Doyle and Howard M. Branz, “The effect of oxygen contamination on the electronic properties of hot-wire cvd amorphous silicon germanium alloys”, Mat. Res. Soc. Symp. Proc. **910**, in press.

9.0 REFERENCES

1. D.V. Lang, J.D.Cohen, and J.P. Harbison, Phys. Rev. B**25**, 5285 (1982).
2. C.E. Michelson, A.V. Gelatos, and J.D. Cohen, Appl. Phys. Lett. **47**, 412 (1985).
3. K.K. Mahavadi, K. Zellama, J.D. Cohen, and J.P. Harbison, Phys. Rev. B**35**, 7776 (1987).
4 . J.T. Heath, J.D. Cohen, and W.N. Shafarman, J. Appl. Phys. **95**, 1000 (2004).
5. Lang, D.V. in *Thermally Stimulated Relaxation in Solids*, vol. 37 of Topics in Applied Physics, ed by P. Braunlich (Springer, Berlin, 1979), p. 93.
6. Cohen, J.D., in *Hydrogenated Amorphous Silicon*, vol. 21C of *Semiconductors and Semimetals*, ed. by J. Pankove (Academic Press, New York, 1984), p. 9.
7. J.D. Cohen and A.V. Gelatos, in *Advances in Disordered Semiconductors Vol I: Amorphous Silicon and Related Materials*, ed. by H. Fritzsche (World Scientific, Singapore, 1988), pp. 475-512.
8. J. David Cohen, Thomas Unold, A.V. Gelatos, and C.M. Fortmann, J. Non-Cryst. Solids **141**, 142 (1992).
9. T. Unold, J.D. Cohen, and C.M. Fortmann, Mat. Res. Soc. Symp. Proc. **258**, 499 (1992).
10. A.V. Gelatos, K.K. Mahavadi, and J.D. Cohen, Appl. Phys. Lett. **53**, 403 (1988).
11. A.F. Halverson, J.J. Gutierrez, J.D. Cohen, B. Yan, J. Yang, and S. Guha, Appl. Phys. Lett. 88, 071920 (2006).
12. B. Yan, G. Yue, J.M. Owens, J. Yang, and S. Guha, Appl. Phys. Lett. **85**, 1925 (2004).
13. T. Unold, J. Hautala, and J.D. Cohen, Phys. Rev. B**50**, 16985 (1994).
14. Y. Lubianiker, J.D. Cohen, H.-C. Jin, and J.R. Abelson, Phys. Rev. B**60**, 4434 (1999).
15. A.F. Halverson, J.J. Gutierrez, J.D. Cohen, B. Yan, J. Yang, and S. Guha,, Mat. Res. Soc. Symp. Proc.**862**, 481 (2005).
16. A.H. Mahan, Y. Xu, L.M. Gedvilas, R.C. Reedy, H.M. Branz, D.L. Williamson, S. Datta, J.D. Cohen, and B. Yan, Proc. 31st IEEE PV Specialists Conference-2005 (Buena Vista)
17. S. Datta, J. D. Cohen, Y.Xu, and A. H. Mahan, Mat. Res. Soc. Symp. Proc. **862**, A7.2 (2005).
18. D.L. Williamson, G. Goerigk, Y. Xu, and A.H. Mahan, Proceedings DOE Solar Energy Technologies Review Meeting, DOE/GO-102005-2067 (2005) p. 444.
19. A.H. Mahan, Y. Xu, L.M. Gedvilas, R.C. Reedy, H.M. Branz, D.L. Williamson, S. Datta, J.D. Cohen, and B. Yan, Proc. 31st IEEE PV Specialists Conference-2005 (Buena Vista)
20. C. E. Michelson and J.D. Cohen, Phys. Rev. B**41**, 1529 (1990).
21. J. David Cohen, in *Properties of Amorphous Silicon and Its Alloys*, EMIS Datareview series, Tim Searle, ed., (INSPEC, London, 1998), pp. 180-188.
22. M Stutzmann, Philos. Mag. B **60**, 531 (1989).
23. Chih-Chiang Chen, Fan Zhong, J.D. Cohen, Jeffrey C. Yang, and Subhendu Guha, Phys. Rev. B 57, R4210 (1998).
24. Shouvik Datta, Yueqin Xu, A. H. Mahan, Howard M. Branz, and J. David Cohen, J. Non-Cryst. Solids, in press.
25. I.L. Repins, B.J. Stanbery, D.L. Young, S.S. Li, W.K. Metzger, C.L. Perkins, W.N. Shafarman, M.E. Beck, L.Chen, V.K. Kapur, D. Tarrant, M.D. Gonzalez, D.G. Jensen, T.J. Anderson, X. Wang, L.L. Kerr, B. Keyes, S. Asher, A. Delahoy, and B. von Roedern, Prog. Photovolt: Res. Appl. **14**, 25 (2006).